Three-Dimensional Velocity Measurements in the Wake of a Hemispherical Roughness Element Using Plenoptic Particle Image Velocimetry

by

Kyle C. Johnson

A thesis submitted to the Graduate Faculty of
Auburn University
in partial fulfillment of the
requirements for the Degree of
Master of Science

Auburn, Alabama
August 6, 2016

Keywords: hemisphere, flow, Plenoptic, PIV

Approved by

Brian S. Thurow, Department Chair, W. Allen and Martha Reed Associate Professor of Aerospace Engineering
David E. Scarborough, Assistant Professor of Aerospace Engineering
D. Stephen Nichols, Assistant Professor of Aerospace Engineering

Abstract

Plenoptic particle image velocimetry (PIV) was used to perform instantaneous three-dimensional (3D) velocity measurements in the near-wake of a wall-mounted hemispherical roughness element at a Reynolds number (based on roughness height) of 4.57×10^3 and boundary layer to roughness height-ratio of 4.67. The experiment was performed in a refractive index matched flow facility to mitigate laser reflections from the hemispherical surface. Data gathered from this experiment represents one of the first applications of plenoptic PIV. The time-average flow is characterized by a separated shear layer off of the hemisphere, a symmetric recirculation region, and an arch-shaped vortex. In the instantaneous 3D velocity fields, a separated boundary layer and recirculation region with asymmetric characteristics are present. Additionally, arch vortices are found that are both attached and detached to the hemispherical surface, similar to previously studied recirculation arch (RA) vortices. The proper orthogonal decomposition (POD) was applied to both the 3D velocity and 3D vorticity fields. Velocity modes produced features associated with the overall flow whereas vorticity modes produced features associated with the wake. The most energetic POD modes confirm the fluctuations in the boundary layer and recirculation region, as well as suggest the existence of shed arch-shaped vortices.

Acknowledgments

This thesis represents three years worth of research in a ongoing pursuit of a Ph.D. The path has been difficult at times and I have been lucky to receive support from numerous individuals who I would like to acknowledge. My advisor, Dr. Brian Thurow has been an invaluable resource for assisting and guiding me in my research and my role in academia. He is surely one of the most passionate professors I have had in my academic career and I appreciate his emphasis on developing well-rounded graduates who are suitable for entrance into academia or industry. I would also like to thank Dr. David Scarborough and Dr. Stephen Nichols for serving on my committee. The members of the Advanced Flow Diagnostic Laboratory have created a fun and supportive work group that has been crucial to my success in my research. Specifically, I am grateful for Tim Fahringer's software development for reconstructing volumes. At the University of Notre Dame and University of Illinois at Urbana-Champaign, I would like thank Dr. Ken Christensen and Taehoon Kim for their collaboration in the experiments performed in this thesis. This research has been funded by the National Science Foundation, so I would like to thank them for making it all possible. I want to express my gratitude to my family and friends who have supported me in a cross-country move in pursuit to further my education. The transition would not have been possible without the constant support and encouragement of my family, especially my parents Gary and Narda Johnson, as well as my brother Travis Johnson. Finally, I would like to thank Molly Thorvilson. She has, and continues to, inspire and encourage me to achieve my goals, no matter how daunting the task. Her support comes not only in the form of love, but also in the meticulous proofing of my papers. Above all, she is always there for me. To everyone that has helped me along the way: Thank you, I know that I am able to conquer any challenge with the support of my family, friends, and colleagues.

Table of Contents

List of Figures

List of Tables

Nomenclature

$\boldsymbol{\Phi}$	optimized basis function, eigenvectors, modes
$\boldsymbol{\Psi}$	An arbitrary basis
$\boldsymbol{\Upsilon}$	an arbitrary basis
$\boldsymbol{C}$	two-point temporal correlation tensor
$\boldsymbol{u}$	a set of snapshots
$\boldsymbol{V}$	eigenvector comprised of coefficients $a(t_i)$
$\boldsymbol{X}$	a state of (x, y, z, t_n)
λ	eigenvalues
λ	wavelength of light in P
$\mathscr{R}$	a Fredholm Integral Operator
ϕ	spherical coordinate of P
$\phi^{(k)}(x)$	basis functions
θ	spherical coordinate of P
$a^{(k)}(t)$	time functions
D	the domain of interest
K	level of approximation
k	index of modes

P	plenoptic function
R	kernel of $\mathscr{R}$
t	time
t_n	time steps
u	data set
V_x	x position of viewer in P
V_y	y position of viewer in P
V_z	z position of viewer in P
x	data at t
1D	one dimensional
2D	two dimensional
3D	three-dimensional
4D	four dimensional
5D	five dimensional
7D	seven dimensional
AFDL	Advanced Flow Diagnostics Laboratory
KLT	Karhunen-Love transform
LFIT	Light Field Imaging Toolbox
MP	megapixel
PCA	principle component analysis

PIV particle image velocimetry

POD proper orthogonal decomposition

RA recirculation arch

RIM refractive index matched

Chapter 1

Introduction

In modern flow diagnostics, there has been a general trend to less intrusive and non-intrusive diagnostics techniques. Historically, hot film and wire anemometry has been the standard for quantitative measurements of velocity, while various flow visualization techniques have provided qualitative insight to these measurements. Researchers were able to make some connections between the one dimensional (1D)point measurements of the anemometers and the two dimensional (2D) or three dimensional (3D) visualizations. While hot film and wire anemometry is still commonly used today for dense temporal sampling, particle image velocimetry (PIV) is a well-established diagnostic for both industry and academia [2]. Traditional PIV measures planar particle field displacements creating a 2D vector field. This diagnostic is well suited for flows than can be simplified to a 2D problem, however many flows relevant to engineering problems are 3D in nature. An example is flow over a highly curved body.

There have been a number of non-intrusive diagnostic techniques to measure 3D flows, each with pros and cons. A widely used technique is stereoscopic PIV, which uses two cameras to create a two dimensional-three component (2D-3C) measurement [3]. Simply put, stereoscopic PIV produces a measurement similar to the planar measurement from traditional PIV with the addition of an out-of-plane component. Although this is an improvement over traditional PIV, it is difficult to capture the flow physics of highly 3D flows. Researchers have simply added more cameras, using four to six cameras to produce a 3D-3C measurement using tomographic PIV [4]. Another technique, synthetic aperture PIV, requires at least five cameras, although eight are commonly used [5]. However, many facilities cannot accommodate this many cameras prompting researchers to consider single camera options.

Plenoptic PIV [6], which is used in this study, falls into this category along with holographic PIV [7, 8] and defocusing PIV [9]. Each technique has its own strengths and weaknesses, and it very well may be that one 3D PIV technique will never be the industry wide standard.

The research presented in this thesis is concerned with flow of a turbulent boundary layer over a hemispherical roughness element. This flow is similar to many real life flows, such as domed buildings or aircraft rivets, but has been specifically modeled after a smooth river rock in a river bed. The hemispherical body has a radius of 12.7 mm, so imaging the flow both over and around the hemispherical body would be difficult with any of the previously mentioned diagnostic techniques. Thus, this work uses a single camera, 3D-3C technique known as plenoptic PIV to measure the flow. The critical component of plenoptic PIV is the plenoptic camera which captures the entire light field of a scene, recording both the angular and spatial information of light entering its aperture. When utilized for PIV, a plenoptic camera can record a relatively cubic volume with a single camera, described in detail by Fahringer, Lynch, and Thurow [6]. This study marks the first extensive application of plenoptic PIV for 3D flow field measurements. This technique is implemented on a refractive index matched (RIM) flow facility. The RIM facility is a free-surface recirculatory tunnel developed by Blois *et al.* [10], with a working fluid of a sodium iodide solution that has an index of refraction identical to the acrylic hemisphere model used for experimentation. This allows the laser used for illumination in PIV to pass directly through the hemisphere-fluid interface with minimal scattering. This unique collaboration of two novel experimental devices allowed for observation of the 3D flow topology in the wake of a hemispherical roughness element, which had not been observed directly with 3D velocity measurements. This experiment was defined as a precursor to future studies of the 3D flow morphology of both impermeable and permeable beds, using the plenoptic camera and the small-scale RIM facility. The objective of this thesis can be summarized in two parts. First, this thesis aims to successfully implement plenoptic PIV for quantitative 3D flow measurements. Second,

this thesis studies the 3D topology of large-scale vortices in the wake of a hemisphere to better understand the flow physics.

Chapter 2

Background

2.1 Light Field Imaging

Before understanding a plenoptic camera, it is important to understand what it is capturing: the light field. Levoy formally defines the light field, or photic field as "radiance along rays in empty space" [1]. It serves well to closely examine this definition.

First, consider the phrase *light field*. It is natural to think that light flows through an environment, but Michael Faraday first suggested that light should be interpreted as a field, in a lecture titled *Thoughts on Ray Vibrations*, summarized in a letter which NASA hosts online [11]. By treating light as a field, Adelson and Bergen, set out to mathematically describe this field [12]. Citing Leonardo da Vinci for their inspiration, Adelson and Bergen begin by asking what can potentially be seen by an observer. The answer is defined as the plenoptic function. Adelson and Bergen consider the plenoptic function to be a complete holographic representation of the visual world, allowing for reconstruction of every possible view, at every moment, from every position, and at every wavelength. Thus, the plenoptic function P is expressed as

$$P = P(\theta, \phi, \lambda, t, V_x, V_y, V_z) \tag{2.1}$$

where *theta* and *phi* represent the spherical coordinates of light seen from a viewpoint, λ is the wavelength of the light seen from a viewpoint, t is the time that the light is seen from a viewpoint, and V_x, V_y, and V_z are the Cartesian coordinates of a viewpoint. Thus, the plenoptic function is a seven dimensional (7D) function.

Next, consider the definition of *radiance*: the amount of light traveling along a ray. Radiance is denoted by L and has units of watts per steradian per square meter ($\mathrm{W} \cdot \mathrm{sr}^1 \cdot \mathrm{m}^2$).

By considering the plenoptic function for radiance and a single instant in time, the plenoptic function is averaged over the wavelengths and reduced to the five dimensional (5D) function given by

$$L = L(x, y, z, \theta, \phi) \ . \tag{2.2}$$

Levoy notes that, if nothing is blocking the ray, the radiance along the ray remains constant. This leads to a redundancy of the 5D plenoptic function. The plenoptic function can be reduced to a four dimensional (4D) function using two-plane parametrization, shown below in Figure 2.1.

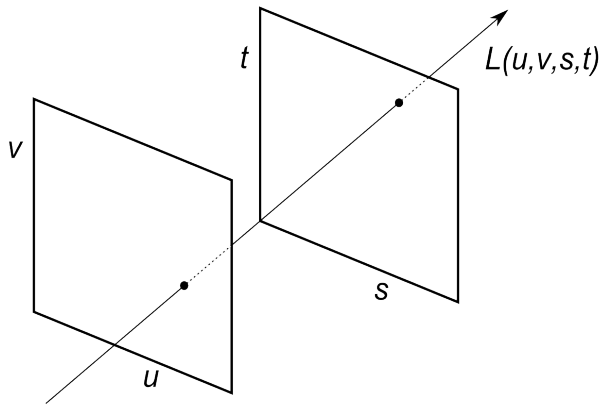

Figure 2.1: Two plane parametrization of the plenoptic function for radiance adapted from Levoy [1]

Many different methods have been proposed to record the light field. Perhaps the simplest to imagine is moving a camera all around a scene, to capture many different views. For this application to work, the scene would have to remain completely stationary, as a technician moved the camera around to gather many different views. A logical improvement to this technique is to use multiple cameras, so that many different views can be captured at the same time. Photographers and cinematographers will use arrays of cameras to capture many different views of a scene at an instant in time, so that the scene does not have to be stationary. These camera arrays can quickly grow very large, requiring many cameras, which is both expensive and difficult to operate. If the range of viewpoints does not span

more than a couple centimeters, we can replace the array of cameras, with a single camera and an array of lenses. First suggested by Gabriel Lippmman in 1908, a sensor behind an array of lenses (microlenses) records a different perspective view of the scene depending on the position of the microlens in the array. Using the two plane parameterization, this records a light field with a uv resolution depending on the number of microlenses and st resolution depending on the number of pixels behind each microlens [13, 1]. If a standard lens is placed in front of the microlens array, focusing the light onto the microlens array, the light field is transposed such that the uv resolution depends on the number of pixels behind each microlens and the st resolution depends on the number of microlenses. This is the basis of a plenoptic camera. A schematic showing a 2D comparison between a conventional camera and a plenoptic camera is seen in Figure 2.2. In a conventional camera, a point source on the world focal plane is focused onto a single pixel, shown in Figure 2.2a. When a microlens array is inserted, angular information is encoded onto the image sensor. To illustrate this effect, light is colored depending on which pixel it strikes behind the microlens. For example, in Figure 2.2b, the light that strikes the bottommost pixel behind the illuminated microlens, comes only from the rays that are emitted from the point source in the range of angles colored purple. Thusly, the same point source is now focused over 8 pixels with the plenoptic camera instead of 1 with the conventional camera.

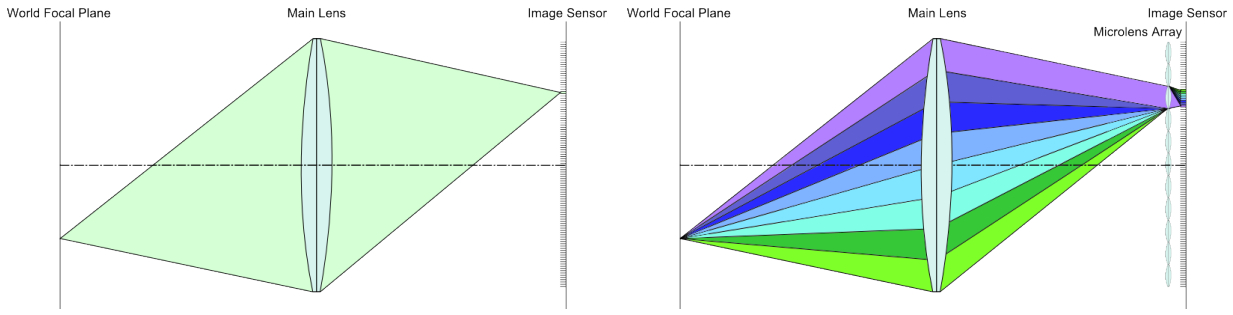

(a) (b)

Figure 2.2: A schematic comparing how a conventional camera (a) and a plenoptic camera (b) record a point source of light on the world focal plane

The plenoptic camera has been limited by resolution. In 1992, Adelson and Wang described and created an early digital camera, but were limited by the technology available. Their camera used a 512×480 pixel image sensor [14]. The camera worked as hypothesized, but the resulting images were only 100×100 pixels, which is not practical for most applications. With improved digital imaging technology researchers at Stanford University were able to create the first hand-held plenoptic in 2005. The plenoptic camera built by Ng *et al.* has a resolution of 4000×4000 pixels which can capture a light field with a resolution of 292×292 in *st* axes and just under 14×14 in the *ut* axes. Ng *et al.* describe the plenoptic camera's most well-known ability to refocus and shift perspective of a scene computationally after the image has been captured.

The plenoptic camera used in this study uses a Imperx Bobcat B4820 conventional scientific camera. The image sensor is a 16 megapixel (MP) TRUESENSE KAI-16000 interline transfer CCD which provides an image resolution of 4904×3280, with square pixels 7.4 microns in size. The microlens array was manufactured by Adaptive Optics Associates, Inc. to have a focal length of 500 microns and a microlens pitch of 125 microns such that there are approximately 16×16 pixels per microlens. A grid of 289×193 microlenses image light onto the image sensor [15, 6]. The physical components of the plenoptic can be seen in the photographs of Figure 2.3. These photographs were taken during the construction of the plenoptic camera. Figure 2.3a shows the microlens array. The physical microlenses are glued to the back of a thick glass slab to allow for easier mounting and positioning of the lenses. The glass slab has a flange around the top edge, opposite to the microlenses, which rests in the microlens mount (MLM) assembly, shown in Figure 2.3b. The MLM assembly is machined out of aluminum at Auburn University consisting of 3 main components: the MLM bracket, the MLM bracket holder, and the MLM cover plate. The microlens array rests in the MLM bracket supported by the glass flange. The MLM bracket is inserted into the MLM bracket holder where it supported by 3 adjustment screws and 3 springs. The MLM cover plate keeps the microlens array in the MLM bracket. The MLM bracket holder

has been designed to resemble a part that is removed from the Imperx Bobcat B4820 such that the two feet on the bracket holder fit securely into the camera body, and the microlens array is straddling the image sensor, seen in Figure 2.3c. This camera was developed as a prototype camera, which has now been replaced by a Imperx Bobcat B6640, which is built around the 29 MP TRUESENSE KAI-29050 interline transfer CCD with an image resolution of 6600 $\times$ 4400. These next generation plenoptic cameras make use of a hexagonally packed microlens array to minimize the amount of unused pixels.

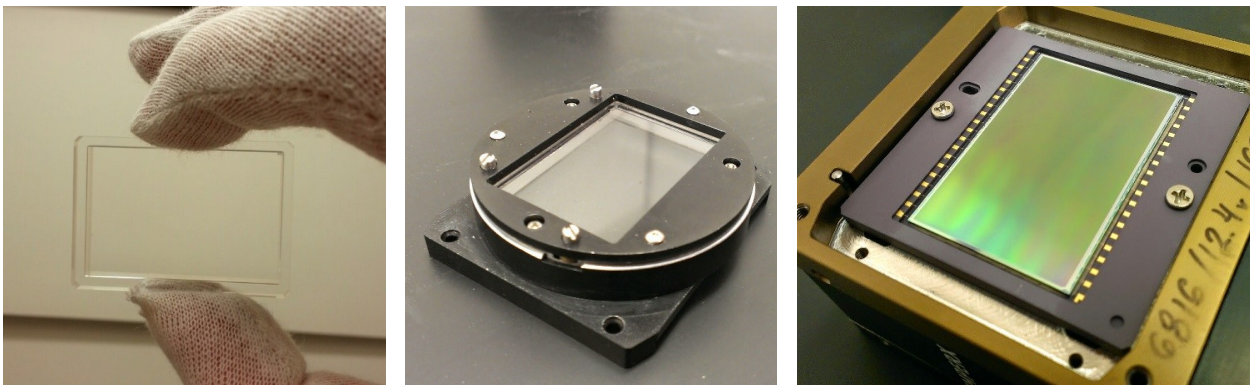

(a) (b) (c)

Figure 2.3: Photographs of: (a) a rectangular microlens array; (b) a custom-designed microlens array mount to accurately position the microlens above the image sensor; (c) Imperx Bobcat B4820 image sensor

A sample image taken with the prototype 16 MP camera is shown in Figure 2.4. The plenoptic camera was set up in the laboratory and objects were placed at various depths throughout the scene. The plenoptic image resembles a normal image but lacks the sharpness. This is due to the microlens array spreading out the light. By examining the inset, it is seen when you zoom in ever further, the letters in "IMPERX" are rather blurry. Also the inset shows the image, or micro-image, formed by each of the microlenses, each circle representing the specific view each microlens has of the aperture. It is clear that the camera is nominally focused on the USA hat.

Figure 2.4: A raw plenoptic image from the 16 MP camera with a rectangular array displaying a scene of objects in the laboratory; the inset shows the micro-images formed by the each of the microlenses

The Advanced Flow Diagnostics Laboratory (AFDL) of Auburn University has constructed several plenoptic cameras for a wide variety of applications, including plenoptic PIV. In the next subsection, §2.2 serves as a brief summary of the plenoptic PIV and the reconstruction technique, which is more completely described by Fahringer *et al.*[6]. To assist with many of the other applications of the plenoptic camera, the AFDL has created the Light Field Imaging Toolbox (LFIT), an open source MATLAB package designed to handle light field images. Some of the main functions include perspective shifts and refocusing, which is demonstrated with the sample in Figure 2.5.

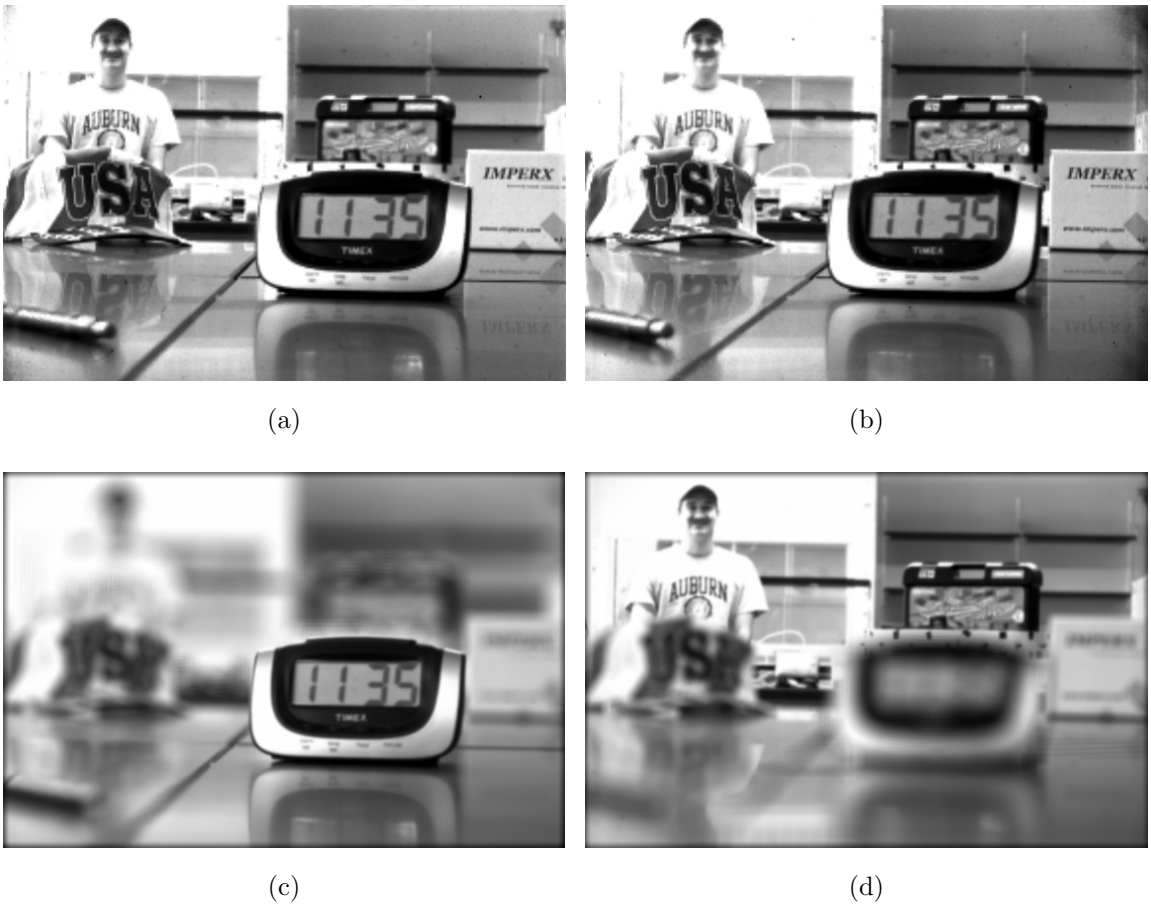

(a) (b)

(c) (d)

Figure 2.5: (a) A left perspective of the scene (b) a right perspective of the scene (c) focused on the alarm clock (d) focused on the researcher in the back of the room

2.2 Plenoptic PIV

The plenoptic camera functions similarly to standard PIV cameras, recording image pairs of an illuminated volume. The images are a two-dimensional (2D) representation of the illuminated 3D volume. Thus, when compared to traditional PIV, there is an additional step of reconstructing the 2D plenoptic images into 3D volumes. Tomographic reconstructions are created using an implementation of the multiplicative algebraic reconstruction technique (MART), similar to the algorithm used for tomographic PIV. The process is detailed by Fahringer, Lynch, and Thurow [6]. This reconstruction technique iteratively solves a system of linear equations that model the imaging system, shown in Equation 2.3. This equation

can be thought of as the projection of the volume intensity distribution $E(x, y, z)$ onto a 2D image $I(x, y)$. However, the reverse of this operation is required to obtain a volume $E(x, y, z)$ from the image $I(x, y)$. Thus, $E(x, y, z)$ is initially defined as a volume discretized into cubic voxels (volume equivalent of a pixel), each with an intensity of 1. Each voxel j can then be projected onto a pixel located at (x_i, y_i), mathematically expressed by

$$\sum_{j \in N_i} w_{i,j} E(x_j, y_j, z_j) = I(x_i, y_i) \tag{2.3}$$

where N_i is the number of voxels in the line-of-sight of the ith pixel and $w_{i,j}$ is the weighting function, which describes what portion of light emitted from a voxel strikes each pixel. The weighting function of a plenoptic camera is different from cameras used in tomographic PIV because the entire volume is not in focus during plenoptic PIV. Thus, a novel approach to create the weighting function was developed by Fahringer, Lynch, and Thurow [6].

Equation 2.4 describes the iterative procedure used to determine a solution for $E(x_i, y_i, z_i)$, known as the MART Equation. Each $k^{\text{th}} + 1$ iteration is defined as

$$E(x_i, y_i, z_i)^{k+1} = E(x_i, y_i, z_i)^k \left(\frac{I(x_i, y_i)}{\sum_{j \in N_j} w_{i,j} E(x_i, y_i, z_i)^k))^{w_{i,j}}} \right) \tag{2.4}$$

where μ is the relaxation parameter which can range between 0 and 1. Convergence is determined by manual inspection of the particle volumes. Fahringer, Lynch, and Thurow present results from this process for both simulated and experimental data [6]. Once the plenoptic data has been reconstructed into a 3D intensity distribution, cross-correlation techniques are applied in an identical fashion to tomographic PIV.

3D calibration was performed using a first order model based on the thin lens equation and estimation of the magnification from imaging of a ruled target. This calibration does not account for higher order effects such as pincushion or barrel distortion associated with real complex lenses. As such, the reconstructed volume is slightly warped compared to the real volume such that the data presented here is considered quasi-quantitative. The

visualizations are expected to accurately identify regions of vorticity and the approximate magnitude of the velocity and velocity gradients; however, a direct comparison with other quantitative measurements will require a higher order volume calibration which is currently under development. Using the same 3D calibration as this study, Fahringer *et al.* report the potential of MART to resolve particle locations to better than 1 voxel in the lateral direction and better than 3 voxels in the depth direction. Errors in particle displacement from a $16 \times 16 \times 16$ voxel cross-correlation were estimated to be 0.2 voxels and 1.0 voxels for the lateral and depth directions, respectively. Thus, the absolute accuracy of the plenoptic PIV measurements made here are limited in comparison to conventional PIV, but are considered sufficient for the visualization and identification of large-scale structures based on the 3D velocity and vorticity fields.

2.3 The Small=Scale RIM

The non-intrusive optical approach to measurement of fluid flows has seen widespread use in a variety of scientific disciplines. However, there exist a number of technologically-relevant flows that are ill-suited for these optical techniques, limited by the presence of a solid phase with a complex geometry (e.g. flow in porous media, internal combustion engines, geophysical flows, etc.). Refractive index matching (RIM) techniques present a solution to allow optical measurements on flow systems of this nature. Blois *et al.*describe that by tailoring the RI of the working fluid in a flow facility to match the RI of the solid geometries to be studied, refraction and reflection of light at solid-fluid interfaces can be diminished [10]. This is the fundamental concept of the Small-Scale RIM flow facility (referred to as RIM facility) constructed at the University of Illinois, Urbana-Champaign. Details on the challenges and design parameters can be found in Blois *et al.*[10]. The RIM facility (pictured in Figure 2.6) is a flow loop designed to recirculate an aqueous solution of $\sim 63\%$ sodium iodide (NaI) that has a RI identical to the acrylic models, 1.495. The NaI solution has the

advantage of having a similar kinematic viscosity to water, allowing a broad spectrum of complex flows to be studied at comparable Re to a standard water tunnel.

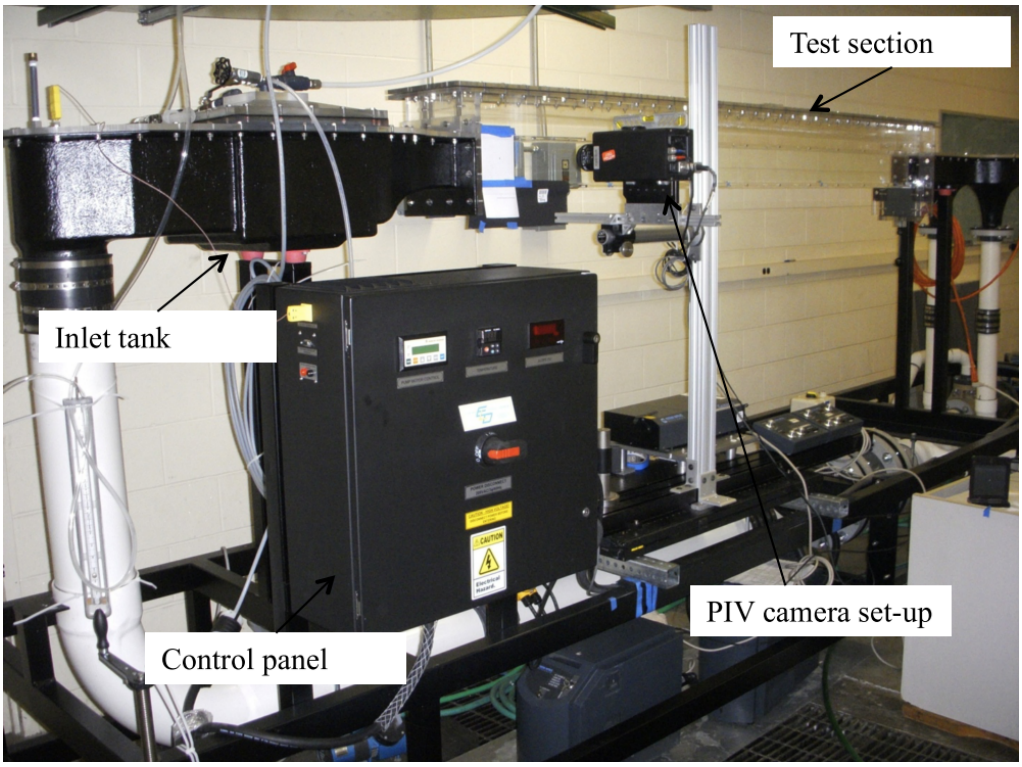

Figure 2.6: Photograph of the Small-Scale RIM flow facility showing a typical PIV system setup

The tunnel test section is constructed entirely of scratch-resistant acrylic, 19.10 mm thick, and is 2.50 m long. The cross-section is 0.1125 m × 0.1125 m with a removable cover that allow for either fully-filled or free-surface conditions to be maintained as well as full access to the interior of the test section for installation of models. The NaI solution is driven by twin fiberglass pumps, capable of producing a combined discharge in the range of $0.016\,\mathrm{m^3\,s^{-1}}$ to $1\,\mathrm{m^3\,s^{-1}}$. When using NaI as the working fluid, additional considerations must be addressed in the design and operation of this RIM facility. The tunnel is slightly pressurized (5 psi) with nitrogen gas (N_2) in order to reduce the discoloration of the NaI solution that occurs when I_3^- ions form due to simultaneous exposure of the solution to oxygen and visible light. The NaI solution must also remain at a relatively constant temperature and is held within a 0.05 °C window which corresponds to a 0.001% change in fluid RI. The

nearly exact RI match of the fluid to the acrylic model allows for the plenoptic camera to image a volume that includes the model, which is crucial to the study of the near-wake structures of a hemispherical roughness element.

2.4 The Proper Orthogonal Decomposition

This thesis revolves around the findings from a relatively large data set, comprised of nearly 1000 volumes. This quantity of data created a need for a procedure to analyze large data sets without rigorously inspecting every volume. The proper orthogonal decomposition (POD) provides a method for extracting synthetic information from large sets of data. The extracted information is synthetic in the sense that it exists only as a representation of the data set as a whole, but does not exist as an individual data sample. The POD is a robust procedure that proves useful in analyzing large data sets from assorted fields.

The study of fluid mechanics has been associated with large data sets for some time now, both computationally and experimentally. The differences in the resolution of these two branches is an important factor when considering the decomposition of a data set using POD. The computational branch is standard in both industry and research as a powerful tool that produces finely sampled data sets with large spatial domains. Although the time resolution of computer generated simulations is highly resolved, it is often too computationally expensive to simulate long temporal periods. Conversely, experimental fluid mechanics are generally associated with extensive time domains that have exceedingly fine resolution. However, data-capturing methods such as hotwire anemometry and laser Doppler anemometry record a relatively small spatial resolution. An outlier in the experimental branch of fluid mechanics is the optical measurement technique PIV, used in this thesis.

Credit for the application of POD to fluid mechanics is given to Lumley [16] who in 1967 used POD to more accurately describe the turbulent flow structures that Townsend [17] originally termed "big eddies." These phenomena are now widely known as coherent structures. Another researcher, A. M. Yaglom, told Lumley in a personal conversation that

POD is the natural idea to replace the usual Fourier decomposition in nonhomogeneous directions. This idea truly was natural because it was a solution reached by many researchers in a wide variety of fields. As a result, this technique is known by an assortment of names, primarily as principle component analysis (PCA) in mathematics, the Karhunen-Love transform (KLT) in signal processing, and the Hotelling transform in multivariate quality control. The process of POD and its many affiliates all share a common goal: representing a data set with a linear combination of orthogonal functions that form the best basis to represent the data.

2.4.1 Basic Math Review

Despite being a relatively simple method to apply, the math behind POD is complex. The less math savvy reader is encouraged to review linear algebra and applied mathematics. The author recommends *Linear Algebra with Applications* [18] and *Applied Mathematics* [19] as a reference. Furthermore, readers that are first beginning POD are referred to *A tutorial on Principal Components Analysis* [20] and *An introduction to the proper orthogonal decomposition* [21]. Emphasis is placed on the covariance matrix [18, 20], the eigenvalue-eigenvector problem [18, 20], the Fredholm integral equation [19], and calculus of variations [19]. A workable example is found in the tutorial on PCA[20].

2.4.2 Overview of POD

The overall objective of POD is to approximate a data set u, defined in Equation 2.5. In this definition, t is the time instance that the data is sampled and x is a the data recorded at each instance, t. In fluid mechanics, this data is often velocity measurements, both two component and three component, or vorticity measurements. The following definitions in this section and the next follow the procedure outlined in The Springer Handbook of Fluid Mechanics [22].

$$u = f(x, t) \tag{2.5}$$

The approximation of u will be written as a sum defined in Equation 2.6, where $\phi^{(k)}(x)$ are basis functions, $a^{(k)}(t)$ are time function coefficients, and K is the number of basis and time functions to be used in the approximation. As $K \to \infty$, this approximation will become exact. This approximation is not exclusive to POD, for example, if the basis functions are defined as functions given *a priori*, Equation 2.6 could define a Fourier series, Legendre polynomials, or Chebyshev polynomials. Alternatively, POD seeks to determine basis functions that are "naturally intrinsic for the approximation of the function $u(x,t)$" [22].

$$u(x,t) \approx \sum_{k=1}^{K} a^{(k)}(t)\phi^{(k)}(x) \tag{2.6}$$

Thus, the general objective of POD is to choose the basis functions $\phi^{(k)}(x)$ and then determine the time functions, $a^{(k)}(t)$, by using the corresponding basis functions, the former being more challenging. The next section defines the approach to defining this naturally intrinsic basis function, which is shown to reduce to an eigenvalue-eigenvector problem.

2.4.3 POD: The Eigenvalue Problem

This section familiarizes the reader with the proper orthogonal decomposition drawing from both *The Springer Handbook of Experimental Fluid Mechanics* [22] and *Turbulence, Coherent Structures, Dynamical Systems and Symmetry* [23]. To begin, let Equation 2.7 denote a set of observations, or snapshots, that exist in the real positive 3 dimensional space. These snapshots are obtained at discrete times throughout the domain of interest, $\Omega(\boldsymbol{x} = (x,y,z) \in \Omega)$

$$\{\boldsymbol{u}(\boldsymbol{X}), \boldsymbol{X} = (\boldsymbol{x}, t_n) \in D = \mathbb{R}^3 \times \mathbb{R}^+\} \tag{2.7}$$

These snapshots could be velocity fields, vorticity fields, temperature, etc. either measured experimentally or simulated numerically, recorded at different time steps or physical parameters (such as Reynolds number). Lumley proposes to extract coherent structures from these random vector fields and defines a coherent structure as "the deterministic function which

is best correlated on average with the realization $\boldsymbol{u}(\boldsymbol{X})$"[16]. Simply put, we seek a function $\boldsymbol{\Phi}$ that has the largest mean squared projection onto the observations. Mathematically, $\boldsymbol{\Phi}$ is the solution to constrained optimization problem defined in Equation 2.8, where $\langle\cdot\rangle$ denotes an averaging operation (temporal, spatial, ensemble, phase average).

$$\max_{\boldsymbol{\Psi}\in L^2(D)} \frac{\langle|(\boldsymbol{u},\boldsymbol{\Psi})|^2\rangle}{||\boldsymbol{\Psi}||^2} = \frac{\langle|(\boldsymbol{u},\boldsymbol{\Phi})|^2\rangle}{||\boldsymbol{\Phi}||^2} \tag{2.8}$$

Here $(\cdot,\cdot)$ and $||\cdot||^2$ denote the L^2 inner product and the L^2 norm, respectively, over D:

$$(\boldsymbol{u},\boldsymbol{\Phi}) = \int_D \boldsymbol{u}(\boldsymbol{X})\cdot\boldsymbol{\Phi}^*(\boldsymbol{X})\mathrm{d}\boldsymbol{X}, \qquad ||\boldsymbol{u}||^2 = (\boldsymbol{u},\boldsymbol{u}) \tag{2.9}$$

where the * represents the complex conjugate. Furthermore, the function $\boldsymbol{\Phi}$ is defined such that

$$||\boldsymbol{\Phi}||^2 = (\boldsymbol{\Phi},\boldsymbol{\Phi}) = 1\ . \tag{2.10}$$

Previously, it was suggested that defining the basis reduces to an eigenvalue problem. The current objective is to show that the solution to the maximization problem defined in Equation 2.8 can be cast in an equivalent eigenvalue problem of the form

$$\boldsymbol{A}\boldsymbol{v} = \lambda\boldsymbol{v}. \tag{2.11}$$

To accomplish this, Equation 2.8 first needs to be modified to the form of the Fredholm Integral Equation, a linear equation defined as

$$\int_a^b k(x,y)u(y)\mathrm{d}y - \lambda u(x) = f(x), \quad a\leqslant x\leqslant b \tag{2.12}$$

by Logan[19]. Here, u is the unknown function, f is a given continuous function, and λ is a parameter. The function k is called the kernel and is given *a priori*. The kernel is assumed continuous on the square $a\leqslant x\leqslant b, a\leqslant y\leqslant b$. If it is required that Equation 2.12 is

homogeneous ($f \equiv 0$) and of the second kind ($\lambda \neq 0$), it follows that

$$\lambda u(x) = \int_a^b k(x,y)u(u)\mathrm{d}y \ . \tag{2.13}$$

This notation can be simplified by using integral operator notation. Seen below in Equation 2.14, K is the Fredholm integral operator. Equation 2.13 can be rewritten as Equation 2.15, which is observed to have the same form as the eigenvalue-eigenvector equation defined in Equation 2.11.

$$Ku(x) = \int_a^b k(x,y)u(y)\mathrm{d}y \tag{2.14}$$

$$Ku = \lambda u \tag{2.15}$$

Returning to the problem defined in Equation 2.8, define a new operator $\mathscr{R} : L^2(D) \to L^2(D)$ as

$$\mathscr{R}\mathbf{\Phi}(\boldsymbol{X}) = \int_D R(\boldsymbol{X}, \boldsymbol{X}')\mathbf{\Phi}(\boldsymbol{X}')\mathrm{d}\boldsymbol{X}' \tag{2.16}$$

where $R(\boldsymbol{X}, \boldsymbol{X}') = \langle \boldsymbol{u}(\boldsymbol{X}) \otimes \boldsymbol{u}^*(\boldsymbol{X}') \rangle$, termed the two-point space-time correlation tensor. The operator $\otimes$ is the dyadic product, such that if a and b are vectors, $a \otimes b = ab^T$. $\boldsymbol{X}'$ represents another snapshot, that may be identical to $\boldsymbol{X}$ but is not explicitly required to be. Here the operator $\mathscr{R}$ is a Fredholm integral operator, the function R is the kernel, and $\mathbf{\Phi}$ is the unknown function. In a general sense, this operator $\mathscr{R}$ is building what amounts to a covariance matrix of a zero-mean data set. This generalization is helpful when implementing POD computationally.

The L^2 inner product $(\mathscr{R}\mathbf{\Phi}, \mathbf{\Phi})$ in Equation 2.17 is expanded to Equation 2.18, then rearranged to form Equation 2.19.

$$(\mathscr{R}\boldsymbol{\Phi}, \boldsymbol{\Phi}) = \left(\int_D \langle \boldsymbol{u}(\boldsymbol{X}) \otimes \boldsymbol{u}^*(\boldsymbol{X}') \rangle \boldsymbol{\Phi}(\boldsymbol{X}') \mathrm{d}\boldsymbol{X}', \boldsymbol{\Phi}(\boldsymbol{X}) \right) \tag{2.17}$$

$$(\mathscr{R}\boldsymbol{\Phi}, \boldsymbol{\Phi}) = \int_D \int_D \langle \boldsymbol{u}(\boldsymbol{X}) \otimes \boldsymbol{u}^*(\boldsymbol{X}') \rangle \boldsymbol{\Phi}(\boldsymbol{X}') \mathrm{d}\boldsymbol{X}' \boldsymbol{\Phi}^*(\boldsymbol{X}) \mathrm{d}\boldsymbol{X} \tag{2.18}$$

$$(\mathscr{R}\boldsymbol{\Phi}, \boldsymbol{\Phi}) = \left\langle \int_D \boldsymbol{u}(\boldsymbol{X}) \boldsymbol{\Phi}^*(\boldsymbol{X}) \mathrm{d}\boldsymbol{X} \int_D \boldsymbol{u}^*(\boldsymbol{X}') \boldsymbol{\Phi}(\boldsymbol{X}') \mathrm{d}\boldsymbol{X} \right\rangle \tag{2.19}$$

Finally, it is seen that Equation 2.19 is reduced to

$$(\mathscr{R}\boldsymbol{\Phi}, \boldsymbol{\Phi}) = \langle |\boldsymbol{u}, \boldsymbol{\Phi}||^2 \rangle \tag{2.20}$$

Observe that the right hand side of Equation 2.20 is identically equal to the numerator of the right hand side of Equation 2.8.

By repeating the steps in Equations 2.17–2.19, it can be shown that

$$(\mathscr{R}\boldsymbol{\Phi}, \boldsymbol{\Upsilon}) = (\boldsymbol{\Phi}, \mathscr{R}\boldsymbol{\Upsilon}) \text{ for any } (\boldsymbol{\Phi}, \boldsymbol{\Upsilon}) \in [L^2(D)]^2. \tag{2.21}$$

The implications of this relationship in Equation 2.21 can be proved using spectral theory or calculus of variations to guarantee the maximization problem in Equation 2.8 has a solution equal to the largest eigenvalue of Equation 2.22. In summary, because of the equality of $(\mathscr{R}\boldsymbol{\Phi}, \boldsymbol{\Phi})$ and the numerator of Equation 2.8 (shown in Equation 2.20 and the relationship shown in Equation 2.21, it is concluded that maximizing $\mathscr{R}\boldsymbol{\Phi}$ will maximize Equation 2.8. As defined in Equation 2.15, the Fredholm operator of the unknown function is equal to the parameter λ times the unknown basis function $\boldsymbol{\Phi}$. It follows that the parameter λ represents the eigenvalues of Equation 2.22, and the basis functions $\boldsymbol{\Phi}$ are the eigenvectors, often called eigenmodes or modes.

$$\mathscr{R}\boldsymbol{\Phi} = \lambda\boldsymbol{\Phi} \tag{2.22}$$

To determine the time coefficients $a^{(k)}$, simply restructure Equation 2.6 to find that the time coefficients are actually projections of $\boldsymbol{u}$ onto $\boldsymbol{\Phi}$. This conclusion is a result of the orthonormality of eigenfunctions $\boldsymbol{\Phi}$, defined below in Equation 2.23. Then $a^{(k)}$ can be found using Equation 2.24. The coefficients $a^{(k)}$ are mutually uncorrelated and their mean square values are the eigenvalues themselves (Equation 2.25.

$$\sum_{i=1}^{n_c} \int_D \Phi_i^{(m)}(\boldsymbol{X}) \Phi_i^{*(n)}(\boldsymbol{X}) \mathrm{d}\boldsymbol{X} = \delta_{mn}; \quad \delta_{mn} = \begin{cases} 0, & \text{for } m \neq n \\ 1, & \text{for } m = n \end{cases} \tag{2.23}$$

$$a^{(k)} = (\boldsymbol{u}, \boldsymbol{\Phi}) \tag{2.24}$$

$$\langle a^{(n)} a^{*(m)} \rangle = \delta_{mn} \lambda^{(n)} \tag{2.25}$$

The basis and the coefficients are now defined and Equation 2.6 can now be used to approximate the data set. As K is increased, the snapshot is projected onto more modes and the approximation becomes more accurate. Because the modes are ranked from the most energy to least, it follows that the approximation is altered less as each successive mode is added to the summation.

This section has described the essence of the proper orthogonal decomposition in the classical approach. The following subsections will outline the procedure for implementing this technique in practice.

2.4.4 Classical Method vs Snapshots Method

Recall in the previous section that the averaging operation $\langle \cdot \rangle$ in Equation 2.8 remains undefined. This section describes the differences between two methods depending on how the averaging operation is defined. The Classical, or Direct, method averages over time while the Snapshots Method averages over space. These two methods are juxtaposed in Figure 2.7. Selecting one method over the other is as straightforward as categorizing the working data set.

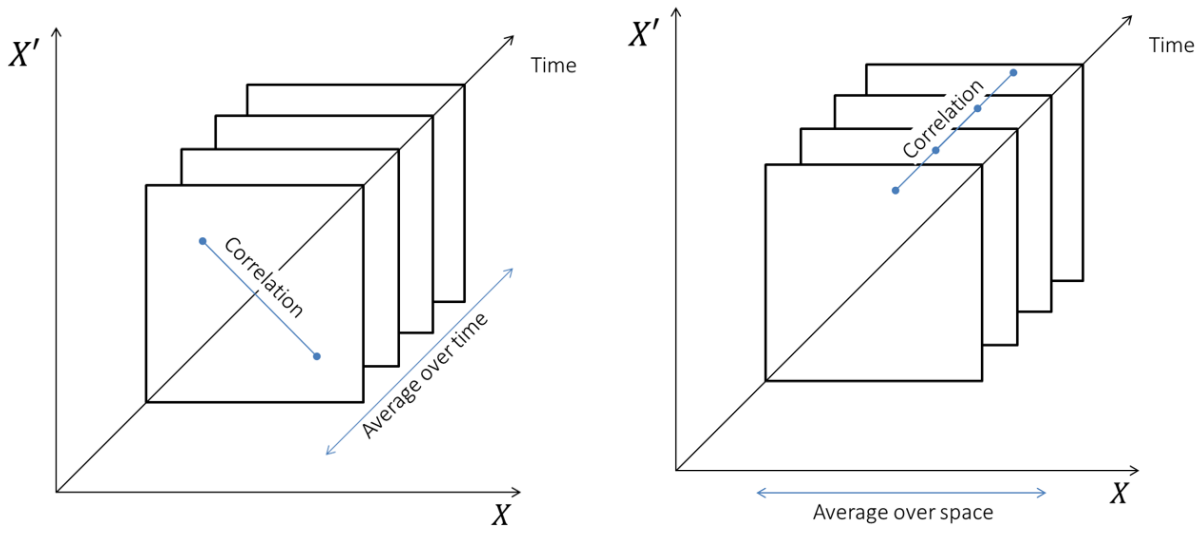

(a) (b)

Figure 2.7: A comparison between two POD methods: (a) Classical Method; (b) Snapshots Method

Regarding fluid mechanics, Classical POD works best for experimental data. The averaging operation is over time, and the correlation is across space, which works well with data gathered using hot-wire anemometry or laser Doppler anemometry. These experimental methods record data at specific spatial locations (often limited by the number of instruments in a measurement array), resulting in a data set with coarse spatial resolution. However, the measurements made by these instruments have a dense temporal resolution. During POD, this high-resolution temporal data is averaged and correlated across the low-resolution spatial data. While Classical POD is best suited for experimental data, Snapshot POD, first suggested by Sirovich in 1987 [24], handles numerical simulation nicely. Data sets from numerical simulation (direct numerical simulation, large-eddy simulation, *etc.*), are usually highly resolved in space and time. However, due to computational cost, the time sample is generally very short. As a result of this constraint, computational data is more densely sampled in the spatial domain than the temporal. Snapshot POD averages this densely sampled spatial domain and correlates the data temporally.

An exception to this categorization is the experimental method, PIV. A typical PIV experiment gathers image pairs, which are correlated to form a data set of velocity vectors taken at different instances in time. A typical experiment could contain data at 1000 time instances, with each instance corresponding to thousands or tens of thousands of velocity vectors. In this way, PIV is more similar to numerical simulation than to the previously mentioned experimental methods.

As shown in Figure 2.7, Snapshot POD is the exact symmetry of classical POD. The mathematical implications of this are straightforward. The difference revolves around the assumption that $\mathbf{\Phi}$ has the form

$$\mathbf{\Phi}(\boldsymbol{x}) = \sum_{k=1}^{N_t} a(t_k)\boldsymbol{u}(\boldsymbol{x}, t_k) \tag{2.26}$$

where the coefficients $a(t_k), k = 1, \ldots, N_t$ are to be determined so that $\mathbf{\Phi}$ is a maximum to the optimization problem previously defined in Equation 2.8. Following the same process, it is shown that the maximum of Equation 2.8 is given by

$$\int_\Omega R(\boldsymbol{x}, \boldsymbol{x}')\mathbf{\Phi}(\boldsymbol{x}')\mathrm{d}\boldsymbol{x}' = \lambda\mathbf{\Phi}(\boldsymbol{x}) \tag{2.27}$$

It follows that the two-point correlation tensor $R(\boldsymbol{x}, \boldsymbol{x}')$ can be estimated assuming stationarity and ergodicity conditions as

$$R(\boldsymbol{x}, \boldsymbol{x}') = \frac{1}{N_t}\sum_{i=1}^{N_t} \boldsymbol{u}(\boldsymbol{x}, t_i) \otimes \boldsymbol{u}^*(\boldsymbol{x}', t_i) \ . \tag{2.28}$$

Finally, substituting the expression of R in Equation 2.28 and the decomposition of $\mathbf{\Phi}$ in Equation 2.26 into Equation (2.27 yields

$$\sum_{i=1}^{N_t}\left[\sum_{k=1}^{N_t}\frac{1}{N_t}\left(\int_\Omega \boldsymbol{u}(\boldsymbol{x}', t_k)\cdot\boldsymbol{u}^*(\boldsymbol{x}', t_i)\mathrm{d}\boldsymbol{x}'\right)a(t_k)\right] \times \boldsymbol{u}(\boldsymbol{x}, t_i) = \lambda\sum_{k=1}^{N_t} a(t_k)\boldsymbol{u}(\boldsymbol{x}, t_k) \ . \tag{2.29}$$

Which can be simplified to

$$\sum_{k=1}^{N_t} \frac{1}{N_t} \left[\boldsymbol{u}(\boldsymbol{x}'.t_k) \cdot \boldsymbol{u}^*(\boldsymbol{x}', t_i) \right] a(t_k) = \lambda a(t_i) \ , \ i = 1, \ldots, N_t \tag{2.30}$$

where the coefficients $a(t_k)$ are defined. Equation 2.30 can be recast as the eigenvalue-eigenvector problem

$$\boldsymbol{CV} = \lambda \boldsymbol{V} \tag{2.31}$$

where

$$C_{ki} = \frac{1}{N_t} \int_\Omega \boldsymbol{u}(\boldsymbol{x}, t_k) \cdot \boldsymbol{u}^*(\boldsymbol{x}, t_i) \mathrm{d}\boldsymbol{x} \text{ and}$$
$$\boldsymbol{V} = \left[a(t_1), a(t_2), \ldots, a(t_N) \right]^T \ .$$

The definition of C is found to be the two-point temporal correlation tensor, which is straightforward to calculate. In direct symmetry to the calculation of the time coefficients in Equation 2.24, the basis function, or modes can be calculated similarly as

$$\boldsymbol{\Phi}^{(n)}(\boldsymbol{x}) = \frac{1}{N_t \lambda^{(n)}} \sum_{k=1}^{N_t} a^{(n)}(t_k) \boldsymbol{u}(\boldsymbol{x}, t_k) \ . \tag{2.32}$$

Fortunately, the application of the POD snapshots method is much simpler than the math behind it. An overview of how the POD has applied to the data set used in this thesis is provided in Chapter 4.

2.5 Flow Physics

Three-dimensional fluid flow over surface protrusions has long been an interest of fluid dynamicists. In general, many experiments in the field pertain to rectangular features, often resembling buildings. The wakes of highly curved bodies, such as hemispheres, have only

been studied by a relatively small number of researchers. However, curved bodies are commonly used in engineering applications, such as surface protrusions on aircraft in aerospace engineering. This study is motivated by roughness effects on the impinging boundary layer, utilizing a hemispherical roughness element to perturb a turbulent boundary layer. The hemisphere model is a simple representative geometry for real surfaces found in nature, such as a smooth rock on the bottom of a river bed.

One of the earliest investigations of the near- and far-wake of a hemisphere was performed by Jacobs in 1938, who traversed a pitot tube to measure pressure[25]. Plots of mean pressure contours depicted curvature of the shear layer and flow separated from the body. Later studies by Kovasznay in 1960 [26] and Klebanoff *et al.* in 1961 [27] were focused on investigating the boundary layer instability using hot wire anemometry and qualitative flow visualization techniques recorded with film cameras. While largely concerned with transition on a smooth plate, both studies also noted that flow over a hemispherical roughness element formed similar structures and behaviors as seen in smooth plate testing. The most striking similarity being that both geometries generated interlacing elongated vortex loops, known as hairpin vortices, first described by Theodore Theodorsen in 1954 [28].

Some of the most influential work on steady flow over wall-mounted hemispheres is that of Acarlar and Smith [29]. Specifically, they studied vortex shedding from a hemisphere within a laminar boundary layer. Using hot film anemometry, hydrogen bubbles, and dye injection, the vortical structures created by the hemisphere were defined qualitatively and quantitatively. Acarlar and Smith tested extensively over a Reynolds number (based on roughness radius) range of $120 < Re_r < 3400$. Hairpin vortices were found to shed from the hemisphere at a measurable frequency and the head of one hairpin overlapped the counter-rotating legs of the preceding vortex. The mechanism of formation of hairpin vortices is two-part: the build-up of concentrated vorticity and the release of this vorticity. It was also found that the low-pressure region in the wake of the hemisphere plays a major role in hairpin vortex creation. This low-pressure region causes the outer irrotational flow field to

curve inward, narrowing the region between the separated boundary layer and the wall. As a result, the free shear layer is curved and causes vortex lines to concentrate and form hairpin vortices. When the vorticity is concentrated, it is shed into the main flow as a discrete hairpin vortex. The downstream evolution of the hairpin vortex consists of the cancellation of vorticity in the legs until they dissipate and the growth of the hairpin head as it moves vertically out of the boundary layer. In addition to the hairpin vortices, Acarlar and Smith also identified a standing, or horseshoe, vortex that is created at the upstream stagnation point of the hemisphere. This standing vortex is formed by the roll-up of impinging vortex sheets to form a steady vortex that follows the contours of the hemisphere. This vortex closely resembles the turbulent horseshoe vortex defined by Baker around the base of a cylinder in both a laminar and turbulent boundary layer [30, 31].

Another study devoted to flow over a wall-mounted hemisphere is the work of Savory and Toy [32, 33], which investigated the near-wake of a hemisphere immersed in a turbulent boundary layer. Velocity data was gathered in a dense sampling of the wake with a pulsed wire anemometer, using a blowdown wind tunnel. Visualization of the near-wake was also performed in a recirculating water tunnel using the thymol blue technique. A single hemisphere was immersed in three different turbulent boundary layers, classified as "thin," "smooth," and "rough." The "smooth" and "rough" cases used vorticity generators and in the "rough" case, various roughness elements to perturb the turbulent boundary layer before it impinged on the hemispherical element. The "thin" case used the natural boundary layer of the the tunnel wall. The study used a hemisphere with a 95 mm radius resulting in a boundary layer to roughness height ratio of 1.1. The Reynolds number, 1.4×10^5, was significantly larger than that of this study. At these conditions, Savory and Toy describe a horseshoe vortex, similar to Acarlar and Smith. In the near-wake, Savory and Toy describe a shear layer that interacts with periodically shed vortex loops. Half of the vortex loop is described to propagate over the top of the hemisphere and through the shear layer, while the other half remains connected slightly above the stagnation point on the windward side

of the hemisphere. It appears that these vortices are the same vortices that Acarlar and Smith identified as hairpin vortices, but Savory and Toy suggest a stronger connection to the upstream face of the hemisphere. A computational study by Manhart in 1988 [34] used an identical experimental setup to the "thin" case by Savory and Toy. Manhart used LES to produce computational results, which were analyzed using Karhunen-Loève transform (KLT), also known as the proper orthogonal decomposition. Although the experimental conditions of these studies differ from the present work, the POD modes will be useful for comparison.

Carr and Plesniak studied pulsatile flow over a hemisphere using planar PIV motivated by human vocal fold polyps and nodules [35]. A hemispherical object with a radius 15 mm was placed in flow ranging from $Re_r = 500$ to 3400. For all of the Re_r values, the boundary layer was initially laminar, comparable to the work by Acarlar and Smith. Carr and Plesniak refer to the classically named hairpin vortices described by Acarlar and Smith as shear layer hairpin (SLH) vortices, as to maintain emphasis on origin as well as morphology. Following this naming convention, Carr and Plesniak define recirculation arch (RA) vortex, which has been seen in several studies on other wall-mounted geometries. The RA vortex can be found in ensemble-averaged realizations, the core of which identifies the center of the recirculation zone in the near-wake of the hemisphere. From experimental images, the RA vortex is described as a half of a vortex ring with ends terminating at a solid surface. The RA vortex differs from the SLH vortex, which forms from shear layer roll-up. Additionally, the RA vortex is suggested to remain stationary, where SLH are known to shed downstream. Carr and Plesniak note that the both the SLH vortex and the RA vortex originate from vorticity in the boundary layer on the surface of the hemisphere. Either or both types of vortices can be created when the boundary layer separates. The experiment used two different 2D PIV data sets, one normal to the streamwise wall and one parallel to the streamwise wall, to infer 3D flow characteristics. Using the swirling strength criterion, the study found that when the unsteady flow slows, the RA vortex propagates upstream, possibly due to self-induced

velocity. The findings of a highly 3D vortex in this experiment further illustrate the need to capture 3D flow physics, so instantaneous vortex geometries can be studied in full 3D.

There have been a handful of other studies performed on hemispherical roughness elements, although the previously presented work is the most similar to the current work. Many of the studies involving a turbulent boundary layer impinging on the element do not provide visualization or insight to the coherent structures of the flow [36, 37]. There has also been computational work regarding strictly laminar flow past a hemisphere, but the primary focus is a comparison of mean lift forces with a sphere [38]. Additionally, many researchers are concerned with hemispherical elements that protrude above the boundary layer, commonly involving turrets [39, 40]. Other studies examine wall-mounted cubes, prisms, or arbitrary bodies, illustrating the sensitivity of this class of flow to many different parameters, Reynolds number, geometry, boundary layer characteristics, *etc.*[41, 42, 43]. These studies are useful to review, but lack strong similarities with the experiment presented.

Chapter 3

Experimental Procedure

The hemispherical element was fixed to the side tunnel wall of the RIM facility, with the plenoptic camera positioned outside of the opposite wall. The laser volume entered perpendicularly from the bottom of the tunnel. A schematic describing the configuration of the experimental apparatus and a photograph of the arrangement are presented in Figure 3.1.

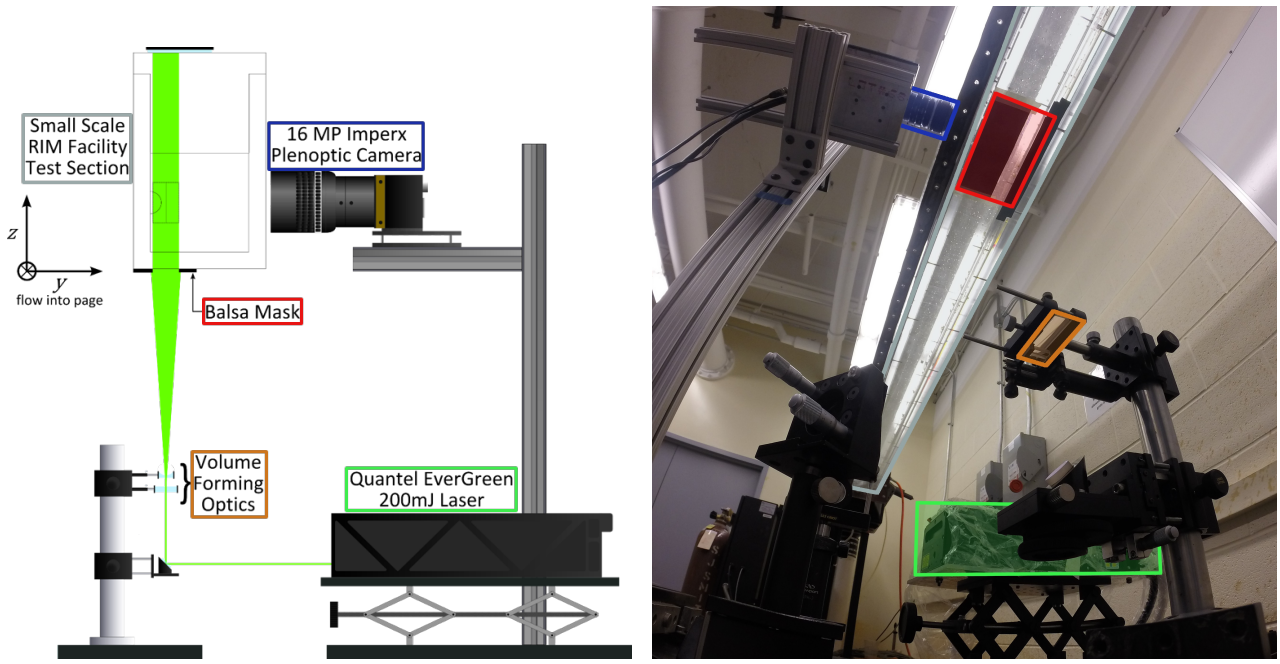

(a) (b)

Figure 3.1: (a) Schematic depicting the experimental arrangement; (b) photograph showing the experimental arrangement, highlighted with same coloring as the schematic in (a)

Illumination was provided by a Quantel (formerly Big Sky) EverGreen 200 mJ double pulse Nd:YAG laser system. The laser beam was spread into a volume using two cylindrical lenses and entered the tunnel along the z direction. A balsa mask clipped the laser in the

y direction and a mirror was placed on top of the RIM facility to increase particle illumination. The resulting interrogation volume has dimensions of 31.5 mm × 30.0 mm × 47.0 mm. The volume was offset 3 mm in the y direction from the wall opposite the plenoptic camera, shown in Figure 3.1a. The dimensions of the volume measured can be seen in Figure 3.2a and Figure 3.2b. The time between laser pulses was set to $\Delta t = 6$ ms, which provided a sufficient range of particle displacement.

The RIM Facility was set to a free stream velocity $U_\infty = 0.396\,\mathrm{m\,s^{-1}}$. At the x location of the measurements, the boundary layer was measured to have a height of $\delta_{.99U_\infty} = 59.3$ mm, corresponding to $Re_\delta = 2.13 \times 10^4$. A single hemispherical roughness element of height $k = 12.7$ mm alters the flow, corresponding to $Re_k = 4.57 \times 10^3$ and $\delta/k = 4.67$. A schematic of the flow field and the hemispherical element is shown in Figure 3.2c. The facility was seeded with silver-coated, hollow glass spheres with a mean diameter of 15 µm and a specific gravity of 1.7, uniquely appropriate for seeding the NaI solution which has a specific gravity of approximately 1.8 while also providing high reflectivity.

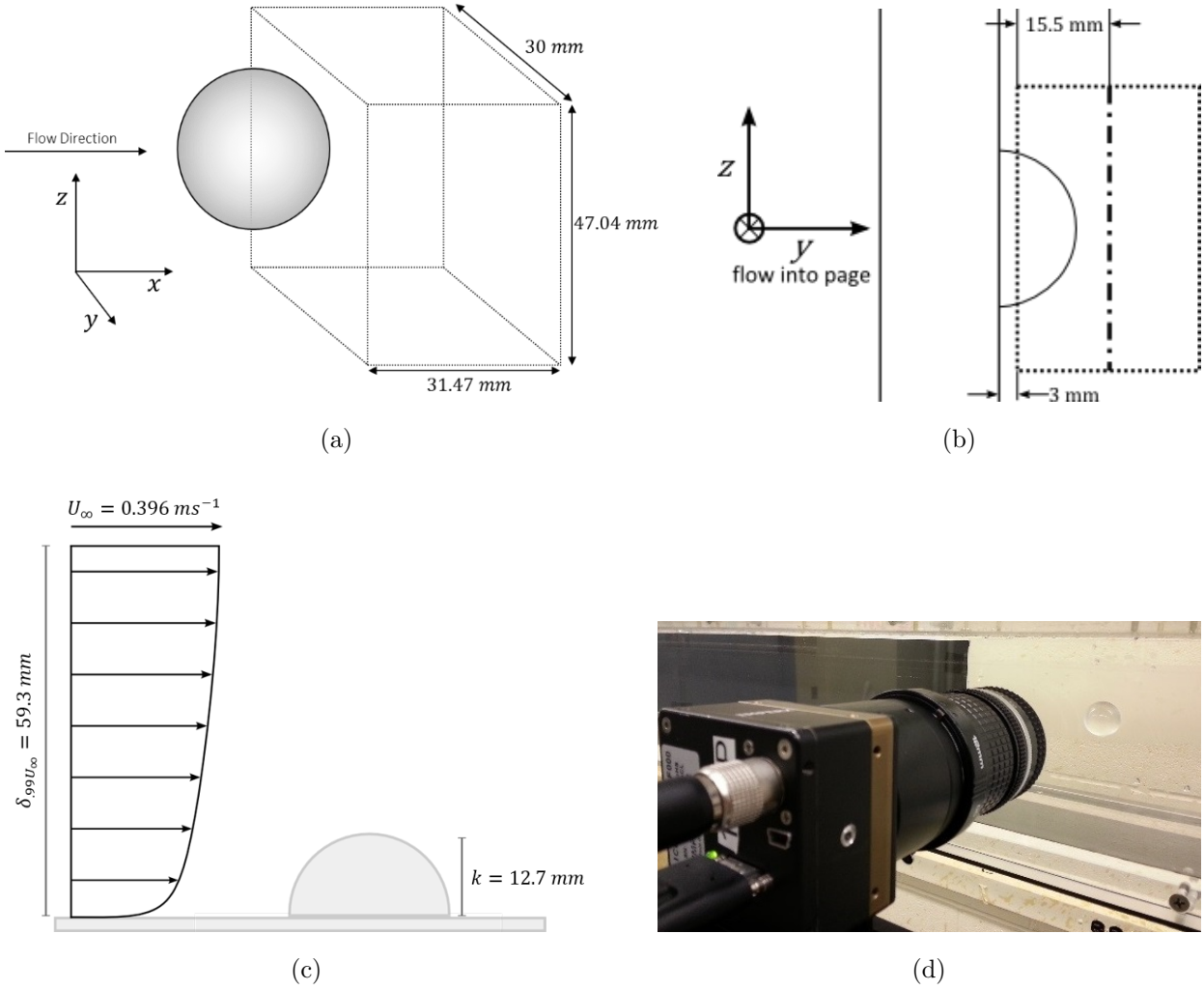

Figure 3.2: (a) schematic detailing the measurement volumes of the near-wake of the hemisphere; (b) a side view schematic to show the focal plane and the 3 mm separation of the measurement volume from the wall; (c) a schematic displaying the size relation of the incoming turbulent boundary layer and the roughness element; (d) a photograph of the plenoptic camera and the roughness element inside the empty RIM facility

The 16 MP plenoptic camera was fitted with a 50 mm prime lens and 43 mm of extension tubes, pictured in Figure 3.2d. The magnification of the optical configuration was -0.765 at the focal plane, in the center of the volume. The f-number of the prime lens was set to $f^{\#} = 2.85$, so that the images formed by the microlenses were touching, but not overlapping. In Figure 3.3, an example of a raw plenoptic image is shown. In the inset, the images formed

by the microlenses can be seen. Using these imaging parameters, 1000 image pairs were captured for the near-wake case.

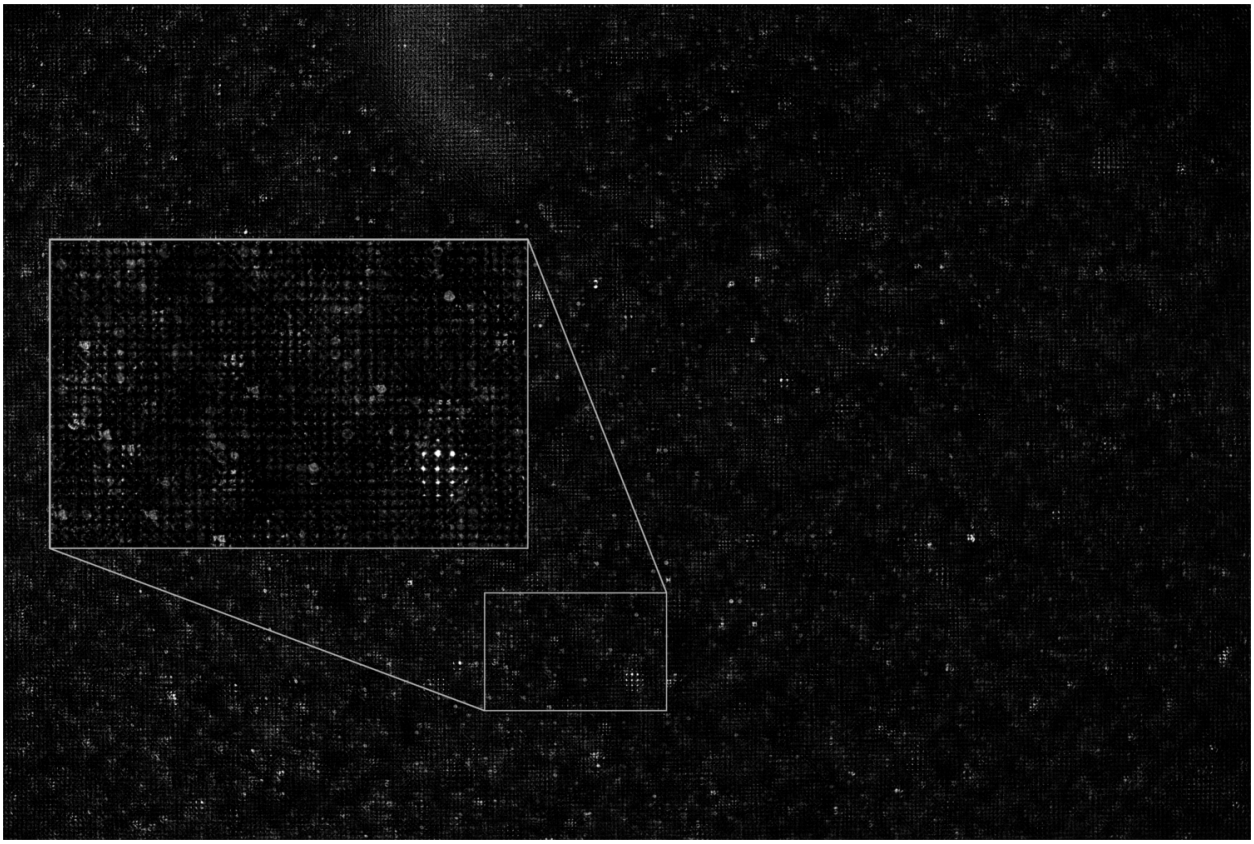

Figure 3.3: A raw plenoptic image from the experimental data set, where flow is from top to bottom; (inset) shows a detailed region where the circular images formed by the microlenses can be seen

Chapter 4

Data Reduction and Analysis

The data gathered was processed in three main steps: tomographic reconstruction using MART, 3D cross-correlation, and the proper orthogonal decomposition. The overall process is summarized in the flowchart in Figure 4.1. The process begins with the 2D plenoptic image pairs, which are reconstructed into volumes using the iterative process MART. Using a cross-correlation algorithm, velocity vector fields are calculated from the volume pairs. The POD is applied to the instantaneous velocity fields, yielding the modes of the data set. These modes represent the velocity fluctuations. In order to better understand and identify the structures of the near-wake, the vorticity is also calculated from the instantaneous velocity fields, and the POD is applied to the three-component vorticity fields. To aid in understanding the physical significance of the higher modes, reduced order projections are formed of the instantaneous velocity and vorticity data onto the respective modes.

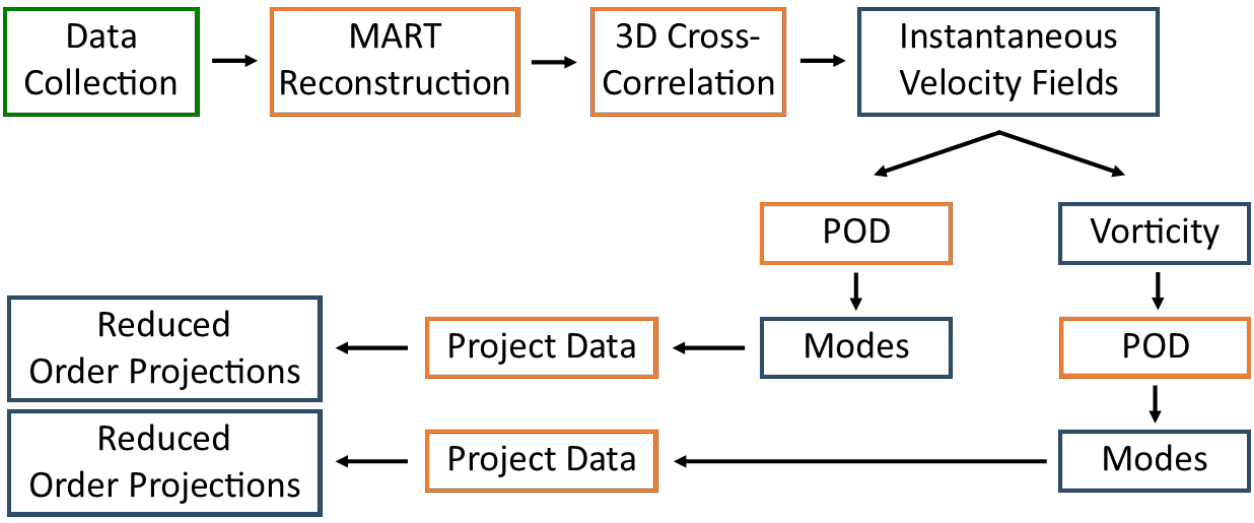

Figure 4.1: Data processing scheme where the green box represents the starting point, an orange box a computational process, and a blue box a result

The tomographic reconstruction using MART, previously described, was the most computationally expensive of the processes. To obtain the particle volumes, 7 iterations were used and the relaxation parameter was set to $\mu = 0.3$. The plenoptic images were reconstructed into a $205 \times 205 \times 300$ voxel grid, based on the volume dimensions shown in Figure 3.2a. The resulting volumes were slightly larger than the measured volume to allow particles to be placed more accurately on the edges of the measured volume, having dimensions of $34\,\text{mm} \times 34\,\text{mm} \times 50\,\text{mm}$. The instantaneous vector fields were calculated using a 3D cross-correlation algorithm which consisted of 4 passes utilizing cubic windows of 64, 48, 32, and 16 voxel sides for each pass, respectively. Each correlation window overlapped the previous, such that the percent overlap for each pass was 25, 33, 25, and 50 percent, respectively. In physical space, the final correlation volume of $2.6\,\text{mm} \times 2.6\,\text{mm} \times 2.6\,\text{mm}$ produces a vector spacing of $1.3\,\text{mm} \times 1.3\,\text{mm} \times 1.3\,\text{mm}$. Vector fields of $24 \times 24 \times 36$ vectors were produced by the final pass, which is a sparser lateral sampling than conventional PIV. This illustrates the main trade-off in plenoptic PIV: a sacrifice of lateral resolution for depth resolution. However, the resulting 3D instantaneous vector field also allows for the calculation of all three vorticity components, which is not possible with conventional PIV methods. Vorticity was calculated using a finite difference method, specifically a second order central difference approximation for calculation of partial derivatives. The vorticity was smoothed with a $3 \times 3 \times 3$ box filter to better emphasize prominent flow features. Each vorticity field was stored such that it complimented its corresponding velocity field, allowing the POD to be applied to both the velocity and vorticity, separately.

The snapshots method of POD was implemented on the vector fields so the modes could be analyzed. Fortunately, the application of POD is straightforward to implement in MATLAB using the *eig* function. In fact, a basic POD algorithm could be written in a few lines of code. In Table 4.1, snapshot POD is outlined in seven steps. Note that the process is agnostic to scripting language and the only necessity beyond basic functionality is a script

to find the eigenvalues and eigenvectors of a matrix. The MATLAB script to that performs these steps can be found in Appendix A.1.

1. Reshape the data into vectors
2. Create a time average of the data (velocity or vorticity)
3. Subtract the time average from all of the data
4. Create the covariance matrix
5. Solve the eigenvalue-eigenvector problem
6. Sort the eigenvalue-eigenvector pairs by descending eigenvalue
7. Calculate the modes and reshape them

Table 4.1: Outline of Snapshot POD algorithm

The first three steps are rather self-explanatory, thus a detailed explanation begins after Step 3, which results in mean-subtracted vectors. The creation of these vectors allows the covariance matrix to be created in step 4 by taking the dot product of all of the vectors. Mathematically, this is written as

$$\text{cov}(\boldsymbol{X}^{(m)}, \boldsymbol{X}^{(n)}) = \boldsymbol{X}^{(m)} \cdot \boldsymbol{X}^{(n)} \ . \tag{4.1}$$

The covariance matrix C has the form shown in Equation 4.2 below

$$C = \begin{pmatrix} \text{cov}(\boldsymbol{X}^{(1)}, \boldsymbol{X}^{(1)}) & \cdots & \text{cov}(\boldsymbol{X}^{(1)}, \boldsymbol{X}^{(s)}) \\ \vdots & \ddots & \vdots \\ \text{cov}(\boldsymbol{X}^{(s)}, \boldsymbol{X}^{(1)}) & \cdots & \text{cov}(\boldsymbol{X}^{(s)}, \boldsymbol{X}^{(s)}) \end{pmatrix} \tag{4.2}$$

where $\boldsymbol{X}^{(1)} \rightarrow \boldsymbol{X}^{(s)}$ represent all of the vectorized snapshots.

The substance of POD is finding the eigenvectors of the covariance matrix, Step 5. Using a program such as MATLAB, the eigenvalue-eigenvector problem in Equation 4.3 is easily solved using a function that inputs the matrix C and returns the eigenvalues λ and

the eigenvectors V.

$$C\boldsymbol{V} = \lambda \boldsymbol{V} \tag{4.3}$$

Sorting the eigenpairs by eigenvalue, in Step 6, identifies the modes. The highest eigenvalue corresponds to the first mode, the next the second, and so on. Finally, in Step 7, calculate each of the modes by projecting the data set onto a basis function, seen in Equation 4.4, which sums the product of the mth eigenvector and every snapshot from the data set.

$$\boldsymbol{M}^{(m)} = \sum_{i=1}^{s} \boldsymbol{V}_i^{(m)} \boldsymbol{X}^{(i)} \tag{4.4}$$

Finally, reshape the modes back to the original dimensions for visualization. Because the data set is vectorized, POD is easily applied to either a 2D or 3D PIV data set with these simple operations.

Chapter 5

Results

5.0.1 Ensemble-Averaged Flow Field

After the images were processed, fourteen pairs were discarded because of poor correlation results, reducing the data set to 986 velocity fields. The ensemble average of these fields is presented below in Figure 5.1a and Figure 5.1b. As presented, the flow is traveling in the positive x direction, traveling over the roughness element which is mounted in the y plane. The streamtraces for this figure, and the following figures, are visualized using Tecplot 360 EX. The streamtraces are calculated using a two-step Runge-Kutta method with a step size of 0.25 times the vector spacing. The streamtraces in Figure 5.1a are colored with the normalized streamwise velocity U^*, with normalization achieved with the free stream velocity, while the spatial directions are normalized by the roughness height k. Streamtraces were regularly placed using two different approaches: one designed to visualize the entire volume and one to visualize the near-wake. For total volume, streamtraces were placed at x/k of 1.5 with 12 streamtraces equally spaced from y/k of 0.1 to 2.2 at every 0.2 z/k; creating 216 streams. The streamtraces propagated in both directions to form the larger image in Figure 5.1a. In the inset, 384 streamtraces were created in the densely packed region behind the hemisphere. Eight streamtraces were placed at three x/k locations (1.2, 1.5, 1.75) equally spaced between y/k from 0.1 to 0.8 at every 0.1 z/k from -0.7 to 0.5, which were propagated in both directions. The dense packing of streams at three different x/k locations aims to capture more of the wake physics in the visualization. The mean flow field shows a recirculation region directly behind the hemisphere, which is in agreement with previous work.[32, 35] The flow separates from the hemisphere surface and approaches reattachment near $2k$ downstream. As y increases, the normalized velocity increases and approaches 1.

Figure 5.1b shows a center slice of the normalized streamwise velocity, highlighting the backflow region, seen in the darker blue. The lighter blue marks the shear layer between the backflow and the turbulent boundary layer, seen in the stratified colors above y/k of 1. Both the streamtraces and the slice of the mean flow field illustrate the ability of the plenoptic camera to resolve different velocities at different depths, as the volume was imaged along the y axis.

The ensemble-averaged field of vorticity magnitude is shown in Figure 5.1c. A red isosurface of higher vorticity sits inside a green surface of slightly lower vorticity. Both surfaces exhibit a curved structure that arches over the region of reverse flow, shown in the blue surface of $U^* = 0$. This ensemble-averaged structure has some resemblance to the definition of a recirculation arch vortex defined by Carr and Plesniak, who define the RA as a time-averaged feature, the center of which defines the center of the recirculation region. The structure shown in Figure 5.1c is more elongated in the x direction than RA vortex sketched and hypothesized by Carr and Plesniak, although the interior red isosurface alone is more similar. However, it is important to remember that Carr and Plesniak used two normal planes of conventional 2D PIV, so 3D structure may not be accurately reflected in their hypothesized sketch.

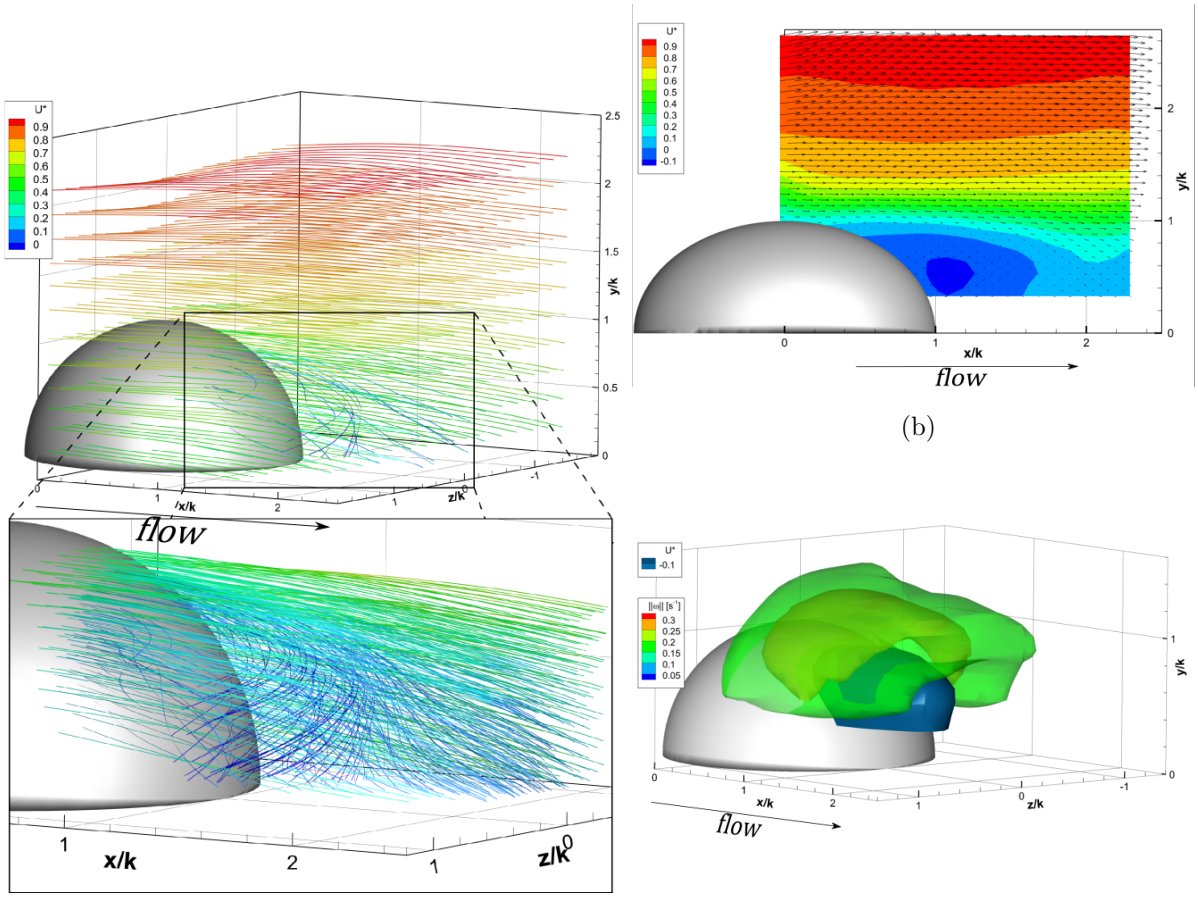

Figure 5.1: (a) Streamtraces of mean velocity field of the near-wake region, colored by normalized downstream velocity; inset shows near-wake streamlines (b) a center slice showing velocity vectors, colored by normalized downstream velocity; (c) ensemble-averaged vorticity magnitude shown with two isosurfaces at $\|\vec{\omega}\| = 0.4, 0.5$ (colored in green and red, respectively) and a ensemble-averaged velocity shown with an isosurface at $U^* = 0$ (colored blue) to highlight the reverse flow

A similar surface is shown in Figure 5.2, the turbulent kinetic energy (TKE) of this data set. A contour isosurface plot is shown that defines an isosurface at each of the colorbar values to better reveal the interior structure of each surface. The highest levels of TKE are concentrated in the near-wake region behind the hemispherical roughness element. The isosurface demarcates a 3D shear layer, having a curved shape similar to the vorticity isosurface in Figure 5.1c. This implies that the shear layer is not only the largest source of vorticity, it also is the most turbulent region of the measurement volume. The greatest

levels of TKE, shown in bright green, extend from the top of the hemispherical element forming the shear layer between the recirculation region and the impinging boundary layer. Although small surfaces exist at the top of the measurement volume, the near-wake shows the highest amounts of TKE, indicating that the hemispherical element is adding energy to the impinging boundary layer.

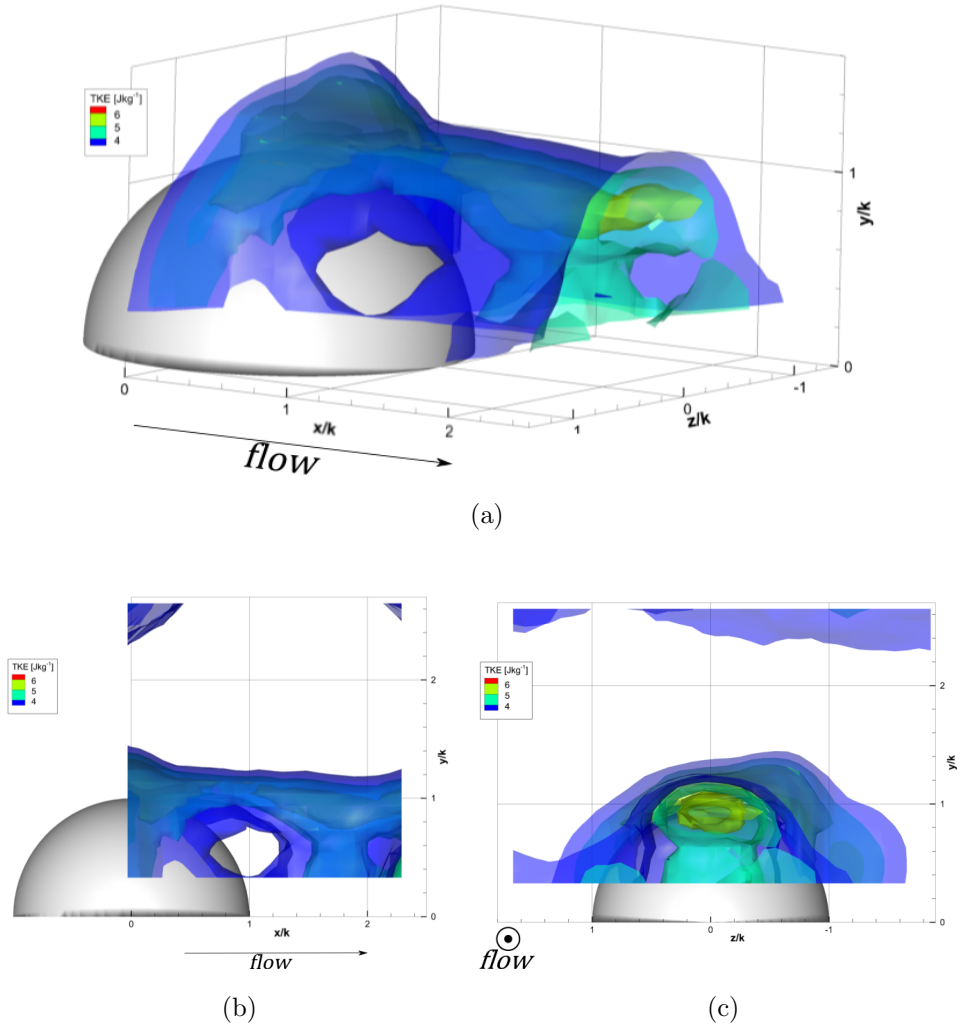

Figure 5.2: Isourfaces at contour levels of ensemble-averaged turbulent kinetic energy (TKE): (a) isometric view; (b) side view; (c) rear view

5.0.2 Instantaneous Flow Fields

The instantaneous velocity and vorticity results show a variety of phenomena, depicting the unsteady nature of the flow. However, the instantaneous volume, shown in Figure 5.3 is

representative of the majority of the realizations. The streamtraces in Figure 5.3a show a recirculation region that stretches from the surface of the hemisphere to the downstream end of the measurement volume at 2.0 x/k. The recirculation region extends to y/k of 0.6, well below the crest of the hemispherical element. As a whole, the region is slightly off-center with respect to the hemisphere, shown by the region of reverse flow in Figure 5.3b centered at about 0.2 z/k. Two small, swirling legs can be seen at the edge of the recirculation region at (x/k, y/k, z/k) location of (0.9, 0.2, 0.6) and (1.5, 0.2, 0.6), seen in the near-wake inset. The legs are more easily identified in the bottom view of the near-wake streams in Figure 5.3b. In the separated flow, the streamlines are relatively uniform with some vertical fluctuation in the boundary layer around 2.0 y/k. An isosurface of vorticity magnitude is shown in the two different views of Figure 5.3c and Figure 5.3d. From Figure 5.3c it is seen the near-wake has a much stronger vorticity on the $+z$ side of the wake and is relatively centered in the z direction. The isometric view, Figure 5.3d, shows the complex structure of the surface, which has a number of legs protruding down on the $+z$ side of the structure. The two largest legs align well with the swirling legs described in the streamtraces. At lower levels of vorticity magnitude, the missing legs of the arch shape on the $-z$ side begin to fill in and the distinct legs on the $+z$ side of the structure become connected. As the structure extends in the downstream direction, it narrows in both the y and z directions as the separated flow moves towards the wall to reattach.

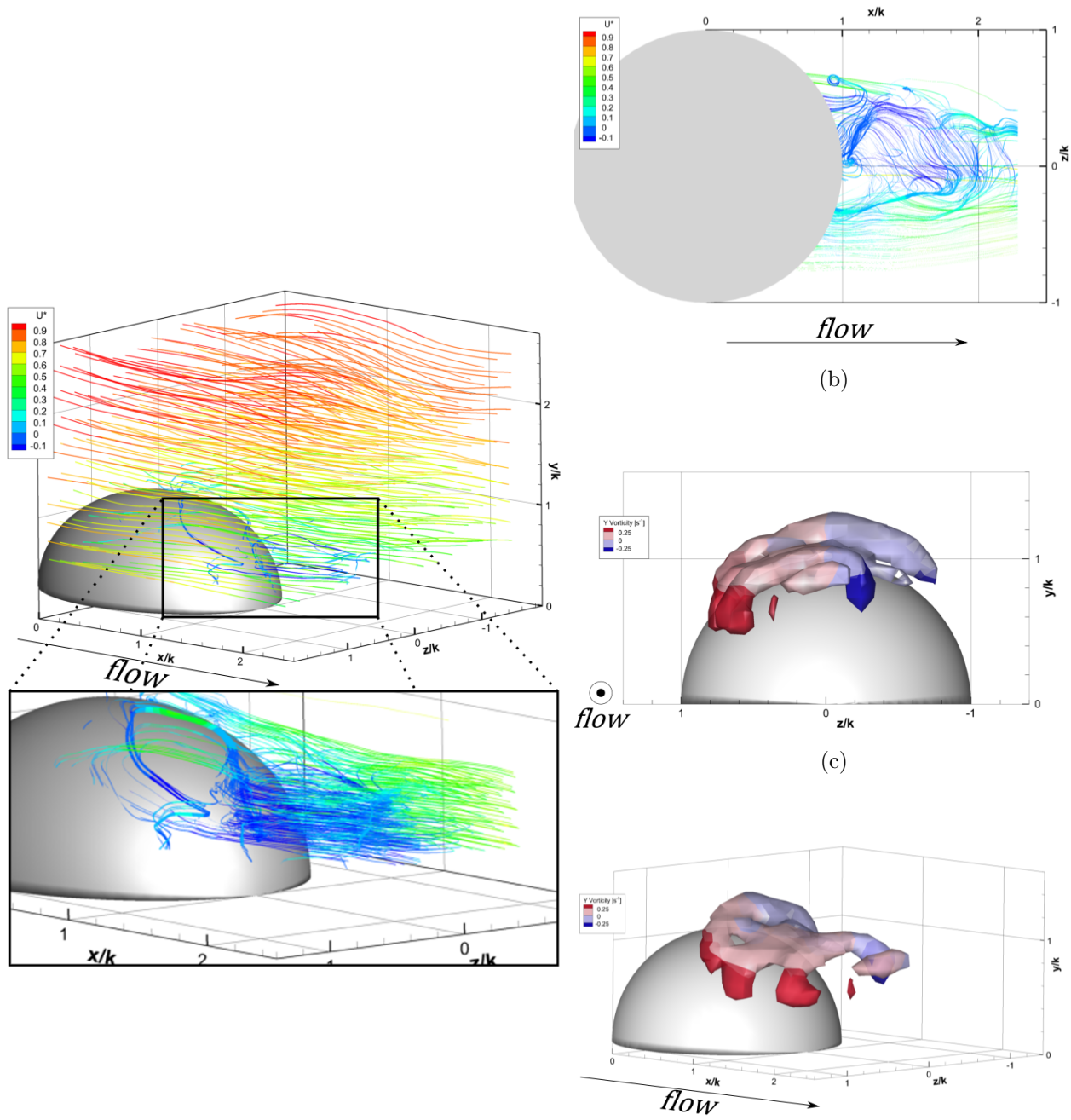

Figure 5.3: Image pair 10 shown using (a) streamtraces colored by normalized streamwise velocity with an inset showing two vortical legs; (b) a bottom view of the near-wake streams depicting the vortical legs (c) an isosurface of vorticity magnitude of $0.33\,\mathrm{s}^{-1}$ shown from the rear; (d) an isometric view of the same isosurface

Variations similar to the instantaneous volume shown in Figure 5.3 exist frequently in the data samples, categorized by a recirculation region that extends towards the downstream

end of the measurement volume. The center of the region of reverse flow and the vorticity magnitude isosurfaces have been seen to fluctuate by as much as ± 0.25 in the z direction. In addition, the top of the surface of the vorticity magnitude plots rarely extends above 1.0 y/k or below 0.7 y/k throughout the data set. This instantaneous volume displays the asymmetric behavior of the near-wake and the broken, asymmetric legs of the arch-shaped vortex. Although RA vortex described in the mean is composed of these arch-shaped legs, it appears that the RA vortex does not frequently, or ever, exist in instantaneous flow. Image pairs such as these are categorized for resembling the ensemble-averaged flow, although there exist some notable exceptions.

In Figure 5.4, two more instantaneous volumes are shown. These volumes show several differences from the previously presented volume. The streamtraces shown in Figure 5.4a, show similar oscillations in the upper boundary layer to Figure 5.3a. A stark difference from Figure 5.3a is seen in the inset of Figure 5.4a, which shows the downward motion of the flow over the hemisphere at about 1.4 y/k. This region of the flow enters the near-wake, suggesting reattachment. The reader is reminded of the 3 mm separation between the wall and the measurement volume when viewing the streamtraces in the near-wake inset, which shows many streamlines terminating at the bottom of the measurement volume. The corresponding vorticity magnitude isosurfaces for this instantaneous volume are shown in Figure 5.4c. An immediate difference between these structures and the isosurfaces in Figure 5.3d is the presence of clusters of high vorticity in the upper boundary layer. In the near-wake, a small arch-shaped isosurface exists, complimented by a curved isosurface, which curves around the hemisphere on the $-z$ side of the volume. The arch-shaped vortex in the near-wake is located where the streamtraces previously described enter the near-wake, suggesting that this arch-shaped vortex is formed by the faster flow entering the near-wake, thereby forcing the recirculation region downward and upstream. High levels of vorticity are created by the shearing between these two opposing motions. A similar effect is seen in the streamtraces flowing around the hemisphere on the $+z$ side in the inset, which intersect the

$+z$ leg of the arch-shaped vortex. A symmetric effect is seen on the $-z$ side of the volume, although it cannot be seen in the inset. The significance of the curved structure around the $-z$ side of the hemisphere is later discussed in the POD analysis in Subsection 5.0.3.

Figure 5.4b shows similar streamtraces to Figure 5.4a, characterized by pronounced perturbations in the upper boundary layer and reattachment. Although the upper boundary layer has large vertical fluctuations, the streamtraces uniformly travel downward near the downstream end of the volume. In combination with the region of streams above the hemisphere that travel downward into the near-wake, similar to Figure 5.4a, this instantaneous volume suggests the flow reattaches at about 2.2 x/k. Unlike Figure 5.4c, Figure 5.4d does not show an arch-shaped isosurface of vorticity magnitude. Instead, larger structures are present in the upper boundary layer and a single, relatively flat structure hugs the hemisphere in the near-wake. The recirculation region is drastically reduced as the reattaching flow has forced the recirculation region upstream and upward. In the inset of Figure 5.4b, a small swirling region of streams is seen in alignment with the isosurface in the near-wake shown in Figure 5.4d. Overall, the two instantaneous volumes shown in Figure 5.4, represent the smaller end of the spectrum regarding the size of the recirculation region and about the upstream maximum of the reattachment point.

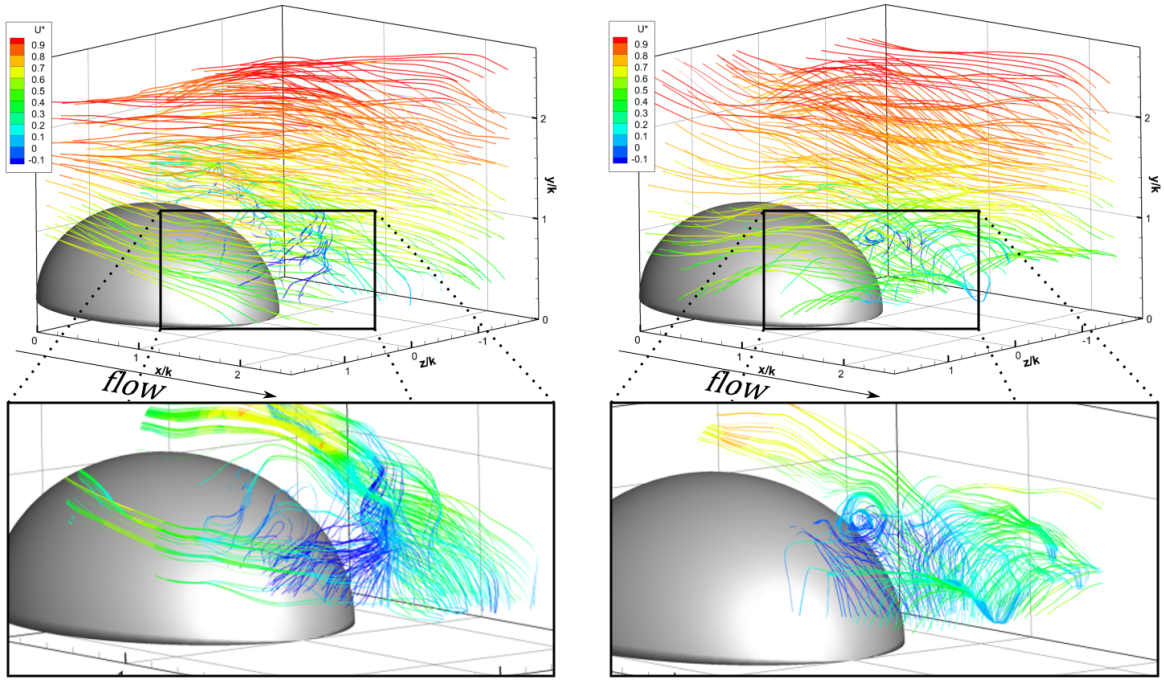

(a) (b)

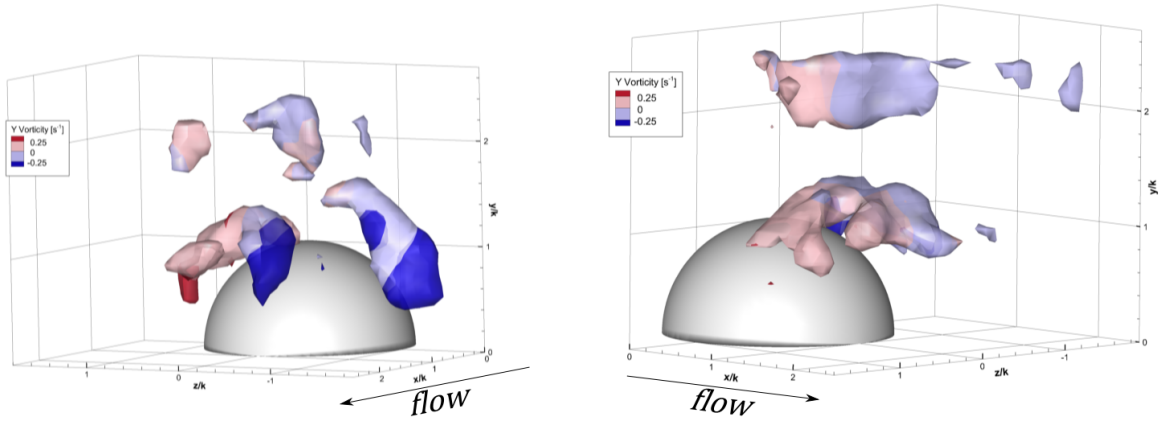

(c) (d)

Figure 5.4: Two instantaneous volumes are shown, 650 and 756: (a) streamtraces of 650 colored by normalized streamwise velocity with an inset showing the wake structure; (b) streamtraces of 756 colored by normalized streamwise velocity with an inset showing the wake structure; (c) an isometric view of an isosurface of vorticity magnitude of $0.33\,\mathrm{s}^{-1}$ of instantaneous volume 650; (d) an isometric view of an isosurface of vorticity magnitude of $0.33\,\mathrm{s}^{-1}$ of instantaneous volume 756;

A well-defined large-scale recirculation region produces the opposite effect by prolonging boundary layer reattachment well outside the measurement volume. These characteristics are present in the two instantaneous volumes compared in Figure 5.5. The velocity streamtraces of the first instantaneous volume, shown in (5.5a, show a recirculation region that extends from the surface of the hemisphere to 1.4 x/k, clinging near to the hemisphere, enlarged in the inset. The isosurface of vorticity magnitude in Figure 5.5c is concentrated in this region. This surface somewhat resembles the isosurface presented in Figure 5.4d, although it is not coupled with any isosurfaces in the upper boundary layer. Although the isosurface is relatively compact, the streamlines in Figure 5.5a do not indicate reattachment in the measurement volume. Figure 5.5b shows the velocity streamtraces for the second instantaneous volume that contains a larger recirculation zone. This expansive region spans from the surface of the hemisphere to the downstream end of the measurement volume. Furthermore, the recirculation zone has a nearly flat peak that is at a constant 1.1 y/k for its entire span, suggesting that the separated flow will remain separated for a prolonged distance downstream. However, the flatness of this feature may be pronounced by the plenoptic camera not having as much sensitivity along the optical axis. This recirculation region is centered at a (x/k, y/k, z/k) location of (1.6, 0.8, 0.0), shown larger in the inset. The vorticity magnitude isosurface in Figure 5.5d is much more expansive than in Figure 5.5c. Again, the vorticity isosurface aligns well with the recirculation area, extending to the downstream end of the measurement volume. The structure of the surface resembles the vorticity isosurface from Figure 5.5c, having some vertical legs, although the isosurface from Figure 5.5d is more contiguous. In contrast to the isosurface in Figure 5.5c, the surface in Figure 5.5b nearly occupies the entire near-wake. Of the well-defined recirculation zones, Figure 5.5b represents the largest of the zones, whereas Figure 5.5a is slightly above average. In combination with the instantaneous volumes shown Figure 5.4, these volumes describe the size variations of the recirculation region. However, the upper bound of the recirculation region size has not been captured by this study, as the downstream end extends outside the measurement volume.

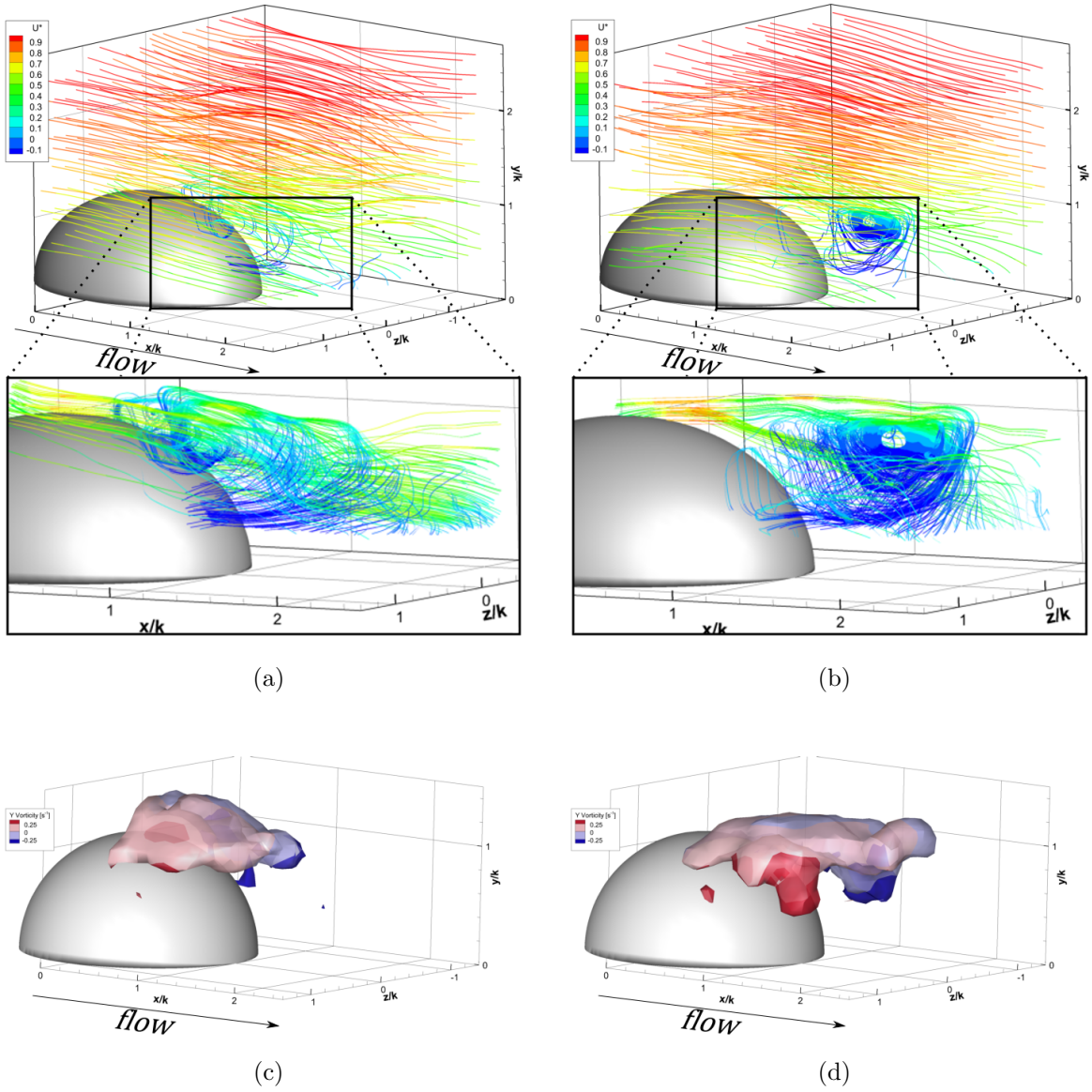

Figure 5.5: A comparison of large-scale recirculation regions, (a) streamtraces of a recirculation zone in image pair 106, shown in detail in the inset; (b) streamtraces of a larger recirculation zone in image pair 253, shown in detail in the inset; (c) isosurface of vorticity magnitude of $0.33\,\mathrm{s}^{-1}$ for image pair 106; (d) isosurface of vorticity magnitude of $0.33\,\mathrm{s}^{-1}$ for image pair 253

The two image pairs shown in Figure 5.6 both contain more definitive arched-shaped structures, showing clear separation from the surface of the hemisphere. The arch-shaped vortex in these image pairs are minimally elongated in the x direction. By manual inspection, approximately fifteen percent of the image pairs have a complete or partial-arch vortex

present in the near-wake flow. This structure is defined by high levels of vorticity, forming an arch shape with counter-rotating legs, which is not connected to the hemispherical roughness element. The image pair shown in Figure 5.6a contains a complete arch and the image pair shown in Figure 5.6b contains a partial arch. In Figure 5.6a, the streamtraces show that the recirculation region extends to at least the downstream end of the measurement volume. The streamtraces flowing over the hemispherical element show that the separated shear layer begins to approach reattachment, seen in the downward motion around $0.8 - 1.0$ x/k and 0 z/k. Then, at 1.5 x/k, the boundary layer turns back up in the y direction, traveling over the peak of the arch vortex. A single vorticity magnitude isosurface shown in Figure 5.6c is colored by y vorticity, and further defines the arch vortex. The structure of the isosurface is clearly an arch, which is consistent with the arch-shaped streamtraces in Figure 5.6a. Despite appearing fairly symmetric, the arch vortex is slightly off center, at -0.1 z/k. In addition, the legs of the arch vortex are not of equal strength. The $+z$ leg is stronger and encloses more volume than the $-z$ leg. The velocity streamtraces of the second image pair, shown in Figure 5.6b, again show a large recirculation region extending to the downstream end of the volume. This instantaneous volume has visible spiraling streamtraces at $(2.0,\ 0.8,\ 0.3)$, which is actually the peak of the arch structure. The vorticity magnitude isosurfaces in Figure 5.6d, depicts a partial arch vortex, which is partially missing a $-z$ leg. The streamtraces show that the region where the $-z$ leg is expected, -0.3 z/k, is dominated by reverse flow in the recirculation region. The partial arch vortex is centered relative to the hemisphere and occurs at nearly the same x location as the complete arch vortex in Figure 5.6a, at 1.8 x/k. In both instantaneous volumes it is seen that the region of reverse flow passes directly through the arch vortex. The arch vortices found by manual inspection consist of both complete and partial arches located at about the same x location and centered anywhere from -0.25 to $+0.25$ z/k. Although the structure in Figure 5.6c resembles the RA vortex sketched by Carr and Plesniak, it is important to note that Carr and Plesniak only hypothesized the RA vortex in the mean, implying it to be stationary. The structure in

Figure 5.6c does not appear to remain stationary, at least over the long sampling frequency of this study, as it is only present in a small number of instantaneous volumes.

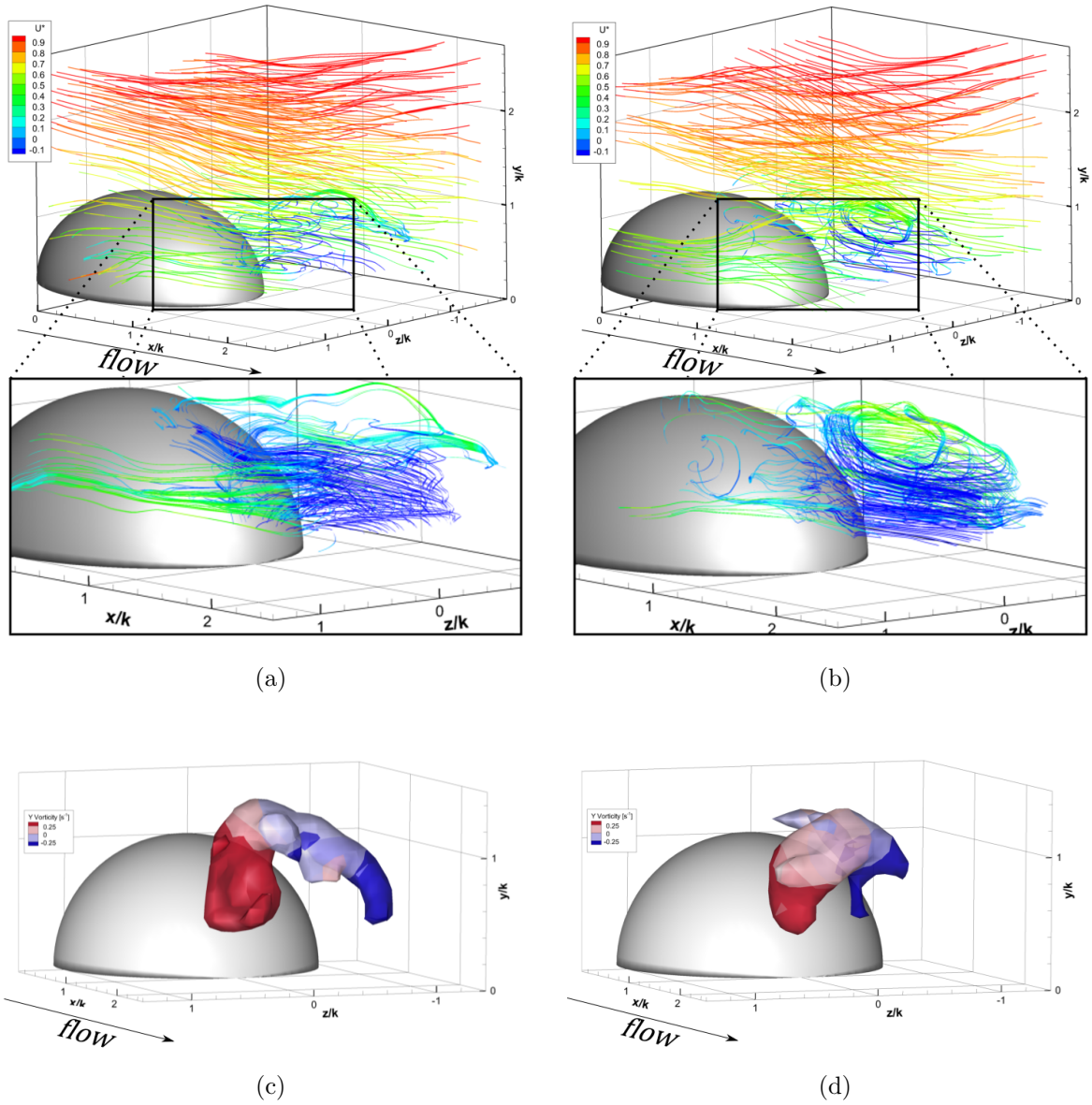

Figure 5.6: A comparison of arch vortices, (a) velocity streamtraces of instantaneous volume 649, shown in detail in the inset; (b) velocity streamtraces of instantaneous volume 575, shown in detail in the inset; (c) isosurface of vorticity magnitude at $0.5\,\mathrm{s}^{-1}$ and colored with y vorticity instantaneous volume 649; (d) isosurface of vorticity magnitude at $0.5\,\mathrm{s}^{-1}$ and colored with y vorticity of instantaneous volume 575

5.0.3 POD Results

The POD analysis of this experiment used both the instantaneous velocity data and the instantaneous vorticity data. The cumulative normalized energy for each the velocity and vorticity modes can be seen in Figure 5.7a. It was found that the first 100 modes of the 986 modes contain about 70 percent of the energy for the velocity case, whereas the first 100 vorticity modes contain less than 50 percent of the total enstrophy. In Figure 5.7b the normalized modal energy for the first 50 modes are shown. It is seen that the first two velocity modes are significantly more dominant than the following modes. Each of the subsequent modes contain less modal energy than the previous by a considerable margin, up to about the 10th mode. After the 10th mode, the modal energy decreases, but the difference between the energy of two consecutive modes is small. An examination of the vorticity modal enstrophy shows that the early modes have very similar enstrophy levels.

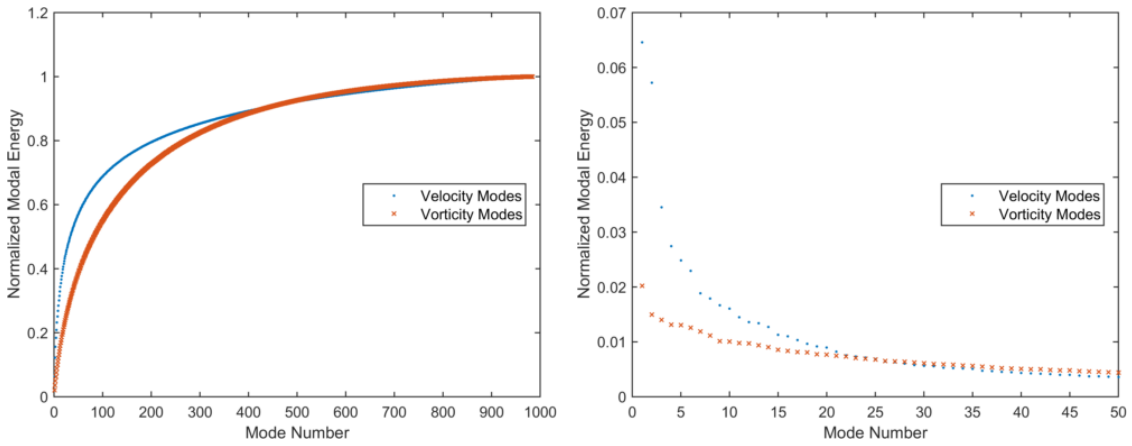

(a) (b)

Figure 5.7: Modal energy plots for velocity and vorticity data, (a) cumulative modal energy for all 986 modes; (b) normalized modal energy for the first 50 modes

The first six velocity modes are shown in Figure 5.8 (at the end of this section). Each mode is presented using isosurfaces of velocity magnitude $||\boldsymbol{U}||$ at 1.1 and a slice through the volume also showing $||\boldsymbol{U}||$. Tangent vectors on the contour slice provide insight to the dominant velocity component of each mode. The first and second modes, Figure 5.8a and

Figure 5.8b, respectively, both describe a similar coupling between the upper boundary layer and near-wake. Both the first two modes are dominated by fluctuations in the y direction, indicating a strong correlation between the boundary layer and the near-wake, although it is difficult to fully define the nature of this relationship. The distinction between the first two modes is blurred by the similar modal energies of 6.46 percent and 5.72 percent, respectively, suggesting that the vertical fluctuations of the upper boundary layer and near-wake oppose each other slightly more often than compliment each other. The first two modes are reminiscent of the first two modes in the study by Manhart [34], showing similar opposing fluctuations from the boundary layer and near-wake. Due to differences between the experiments, the comparison to the modes presented by Manhart is strictly focused on the near-wake region and above. However, it is difficult to tell the y location of the isosurfaces as Manhart provides only a top down view of the modes. Although it is not explicitly shown in Figure 5.8, the u and w fluctuations also resemble the isosurfaces shown by Manhart. Due to the synthetic nature of the modes, understanding the physical implications can be difficult. In Figure 5.9, an instantaneous snapshot has been projected onto the modes to provide insight to the physical significance of the modes. Figure 5.9a shows the original instantaneous volume, which is identical to a projection with 100 percent of the total modal energy. Streamtraces are used to visualize these projections, colored by streamwise velocity. The streamtraces are placed sparsely throughout the volume and densely placed in the near-wake region to better capture the finer details of the near-wake. This snapshot is characterized by large oscillations in the upper boundary layer and the downward motion of the separated shear layer which flows over a small recirculation bubble before heading towards reattachment. When this snapshot is projected onto the first two modes, containing 11 percent of the total energy, the volume appears very organized, seen in Figure 5.9b. The projection shows the downward motion of the upper boundary layer and upward motion in the near-wake. Some influence of the second mode is seen in the variation in the streamtraces in the upper boundary layer that show some vertical perturbations from the overall downward motion attributed to the

first mode. With only two modes, the separated shear layer shows no signs of reattaching as the near-wake shows no downward motion.

The third and fourth modes, Figure 5.8c and Figure 5.8d, respectively, are both dominated by fluctuations in the upper boundary layer. Whereas the first two modes show fluctuations that vary spatially nearly exclusively with y, the third and fourth modes show fluctuations in the upper boundary layer that vary with x, y, and z. The modal energies of the third and fourth modes are significantly less than those of the first two, having 3.45 percent and 2.74 percent of the total energy, respectively. The physical effects of the third and fourth modes can be seen in the projection shown in Figure 5.9c, which uses the first four modes, containing 18 percent of the total energy. As expected, the near-wake closely resembles the near-wake in Figure 5.9b. The influence of the third and fourth modes is seen in the fluctuations in the upper boundary layer, specifically the non-uniformity in the x and z directions. With only 18 percent of the total energy, the upper boundary layer resembles the upper boundary layer of the instantaneous volume. This suggests that the higher modes largely account for the changes in the near-wake.

The fifth and sixth mode are shown in Figure 5.8e and Figure 5.8f, containing 2.48 and 2.29 percent of the total modal energy, respectively. Again, these two modes are of similar structure, consisting of both more and smaller isosurfaces when compared to the previous four modes. Similar to the third and fourth modes, both the fifth and sixth modes show isosurfaces in the upper corners of the volume. However, the fifth and sixth modes show a coupling between these structures and the near-wake, which in both modes is enveloped in a relatively flat isosurface at the bottom of the volume. In both modes, the near-wake has two regions of opposite fluctuations, seen by the vectors in the slices. Additionally, a scattering of isosurface exist in the middle of the volume, vertically, including large isosurfaces enclosing the flow around the hemisphere in the z direction. A stark difference between the modes is seen in the vectors in the slices. The fifth mode shows alternating fluctuations between the four upper corners, suggesting some large-scale circulation motion, whereas the sixth mode

has opposite fluctuations only on the $+z$ side of the volume. Figure 5.9d shows a projection onto the first 6 modes containing 23 percent of the total energy. The primary difference between this projection and the projection with 18 percent total energy in Figure 5.9c is the changes to the near-wake. The streamtraces are now nearly flat across the top of the hemisphere. Compared to the instantaneous volume, the wake is still significantly different. The upper boundary layer is nearly identical to the projection with 18 percent energy. Thus, the physical significance of the fifth and sixth mode can be summarized as slight variation to the upper boundary layer, coupled with larger changes to the near-wake region.

The next thirteen modes each contain between 1 and 2 percent of the total energy, and all following modes are less than 1 percent of the total energy. For brevity, only the first 6 modes are presented in here and Appendix B.2 shows additional higher modes. However, the effects of the higher modes are seen in the projections in Figure 5.9e and Figure 5.9f, which contain 19 modes and 61 modes, respectively. These projections contain 40 and 60 percent of the total energy, respectively. In the 40 percent projection, Figure 5.9e, the streamtraces traveling directly over the hemisphere head down into the near-wake, which is characteristic of the instantaneous volume. Again, the upper boundary layer looks much the same as the previous projection. With 60 percent of the total modal energy, the projection in Figure 5.9f closely resembles the instantaneous volume. Both the boundary layer and wake have visibly changed compared to the previous projection. The upper boundary layer is not more perturbed and is nearly identical to the upper boundary layer in the instantaneous volume. The near-wake still has significant differences from the instantaneous volume, which signifies that the remaining 925 modes will be largely concentrated in the near-wake region, which is also seen by manual inspection. Through this analysis, it is determined that a majority of the energetic modes are characterized by fluctuations in the boundary layer, which may not be a direct influence of the hemispherical roughness element. This motivated a separate POD analysis on the vorticity, as it was hypothesized that the energetic modes

would better describe the effects of the hemispherical roughness element on the incoming turbulent boundary layer.

Returning to Figure 5.7, it is seen that the most energetic modes contain significantly less modal enstrophy compared to the POD of velocity. The first six vorticity modes, shown in Figure 5.10, contain only 8.8 percent of the total enstrophy compared to 23 percent of the total energy contained in the first six velocity modes. The pairing of modes seen in the POD of velocity is not present in these first 6 vorticity modes. Each mode is presented with vorticity magnitude $||\boldsymbol{\omega}||$ isosurfaces which are colored with y vorticity or z vorticity to show the dominant component. The first mode, Figure 5.10a, depicts an extruded arch shape similar to the ensemble-averaged vorticity. This mode contains 2.02 percent of the total enstrophy and is completely concentrated in the near-wake region. The arch shape only extends from 1.4 x/k to 2.0 x/k, as from 0.6 x/k to 1.4 x/k the shape is connected along the bottom, resembling a donut. The opposing y vorticity fluctuations show two counter-rotating legs in this arched structure. The surface is nearly symmetric along 0.0 z/k, except for a bulge in the surface at 0.0 x/k on the $-z$ side and a less defined end of the arched surface on the $-z$ side at 2.0 x/k. A similar asymmetry is seen on the $-z$ side in the second mode, Figure 5.10b. This mode contains 1.50 percent of the total enstrophy and is largely concentrated in the near-wake region, except for two small isosurfaces in the upper boundary layer. The second mode shows a more defined arch shape compared to the first mode, although it is offset in the $+z$ direction, such that the $+y$ vorticity leg is centered behind the hemisphere. The isosurface shows another leg branching off in the $-z$ direction that is at the upstream end of the volume, representing the flow directly over the hemisphere. Although this mode shows three small isosurfaces in the upper boundary layer, it is largely dominated by near-wake structures. This mode suggests a coupling between the vorticity of the flow directly over the hemisphere to the superposition of the arch vortex. Similar in structure, the third mode, Figure 5.10c, has 1.40 percent of the total enstrophy. The arched vortex in this mode is larger than the previous and has a smoother, more regular

arch shape. Additionally, the arch vortex is symmetric and centered about 0.0 z/k. It is worth noting that this arch structure is reminiscent of the RA vortex sketched by Carr and Plesniak, even more so than the vortex previously presented in the instantaneous volume pair. As in the second mode, a similar curved isosurface exists over the $-z$ side of the hemisphere in the third mode. This suggests that the superposition of the arch vortex is not dictated by an increase of vorticity of the flow directly over the hemisphere. The relatively small difference in percent of total enstrophy between the two modes also suggests that the modes are closely related. This superposition of the arch-shaped vortex has been seen in the instantaneous pairs, although the arch vortex is rarely as well-defined as in these modes. Unlike the first three modes, the fourth mode, Figure 5.10d, is composed of isosurfaces in the upper boundary layer. These structures are each dominated by x vorticity, which is shown on the colorbar. This mode has 1.31 percent of the total enstrophy. The small structure in the near-wake is largely constituted of z vorticity, possibly representing the top of an arch vortex. This mode represents the motivation of calculating the POD of the vorticity components, as it is possible these structures originate from the incoming turbulent boundary layer and are not directly seeded into the flow by the hemispherical roughness element, whereas the earlier modes are clearly generated by the hemisphere. The fifth mode, in Figure 5.10e, again shows the superposition of the arch-shaped vortex, this time offset in the $-z$ direction. This mode is nearly equivalent to the fourth mode in enstrophy, containing 1.30 percent of the total enstrophy. Interestingly, this superposition is not coupled with a fluctuation in the flow traveling around the hemisphere; suggesting that they are independent events. The three isosurfaces in the upper boundary layer are analogous to the the isosurfaces in the fourth mode and, when colored by x vorticity, follow the same pattern. The sixth mode, Figure 5.10f, contains 1.26 percent of the total enstrophy and shows a combination of structures in the upper boundary layer and the near-wake. The isosurfaces in the near-wake are formed by concentrated y vorticity, whereas the isosurfaces in the upper boundary layer are composed of both x vorticity and z vorticity. The near-wake does not contain

any arch-shaped structures, which are no longer prominent in any of the subsequent modes. Additionally, the structures in the near-wake region and the upper boundary layer continue to get smaller in the subsequent modes.

Due to the comparatively small amounts of total enstrophy in the higher vorticity modes, the reduced order projections presented in Figure 5.11 use more modes than the corresponding POD results of velocity. Figure 5.11a shows the instantaneous volume having 100 percent of the total enstrophy of the volume pair. Vorticity isosurfaces are calculated in the identical manner to the isosurfaces in the vorticity modes. This instantaneous volume has been selected for its resemblance to both the second and third vorticity modes, which shows an arch-shaped vortex and a higher vorticity leg on the $-z$ side of the hemisphere. Additionally, several structures are scattered throughout the upper boundary layer. In Figure 5.11b, the the volume pair is projected onto the first four modes, containing only 6 percent of the total enstrophy. The projection shows a single isosurface that is arch-shaped at the downstream end and flares upward at the upstream end. It is interesting that none of the upper boundary layer structures have been created by the fourth mode; suggesting that the physical processes that creates the structures in this volume and the fourth mode are likely different. In Figure 5.11c, the first 8 modes are used, accounting for 11 percent of the total enstrophy. Visually, not much is changed from the previous projection, although twice the number of modes have been used. In Figure 5.11d, 18 modes are used, accounting for 20 percent of the total enstrophy. This projection again shows a single surface where the arch shape at the downstream end is slightly reduced and the flow around the $-z$ side of the hemisphere is accented as it begins to resemble the instantaneous volume pair. With 40 percent of the total enstrophy, Figure 5.11e shows the instantaneous volume pair projected onto the first 54 modes. Again, the projection shows a single surface, which bears much more resemblance to the second and third vorticity modes now, despite being a combination of many more modes. Still, even with 40 percent of the total enstrophy, no structures exist in the upper boundary layer. Finally, in Figure 5.11f, the projection shows isosurfaces in the upper boundary layer.

This projection uses the first 122 modes and contains 60 percent of the total enstrophy. Thus, as predicted, the POD of the vorticity has produced modes with an emphasis on the enstrophy of the near-wake structures. This projection also strongly resembles the second and third modes, which is a physical indication that, although an increase of vorticity in the flow around the hemisphere does not necessarily correspond to a more defined arch-shaped vortex in the near-wake, the two events can occur simultaneously.

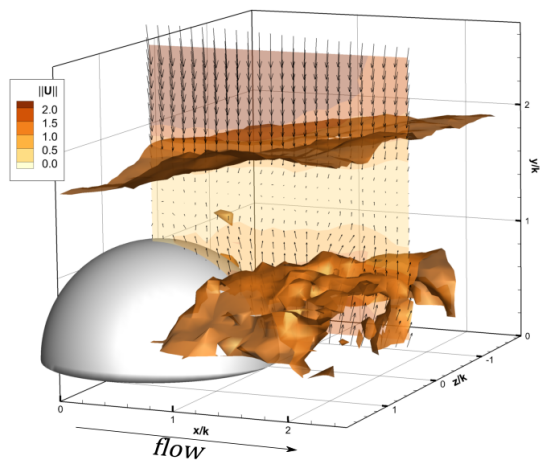

(a) Mode 1

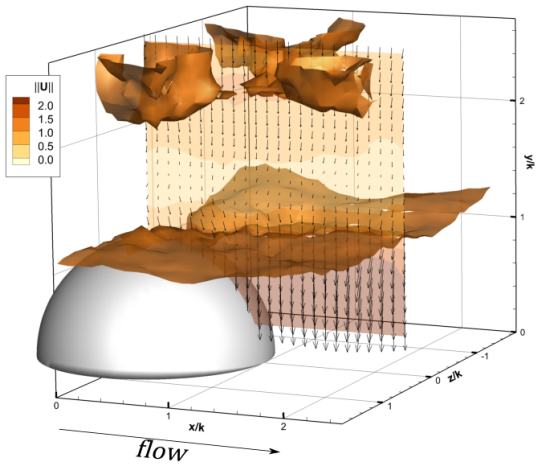

(b) Mode 2

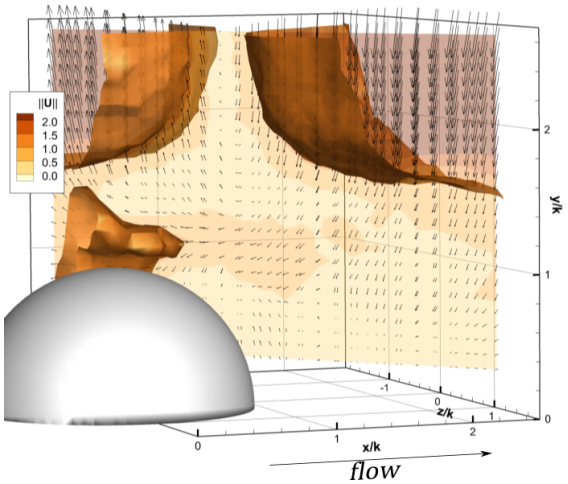

(c) Mode 3

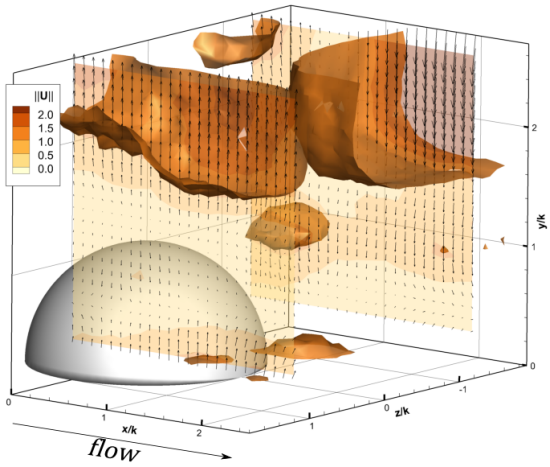

(d) Mode 4

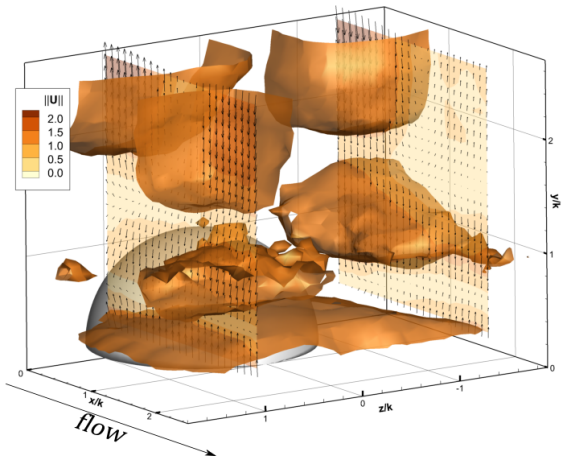

(e) Mode 5

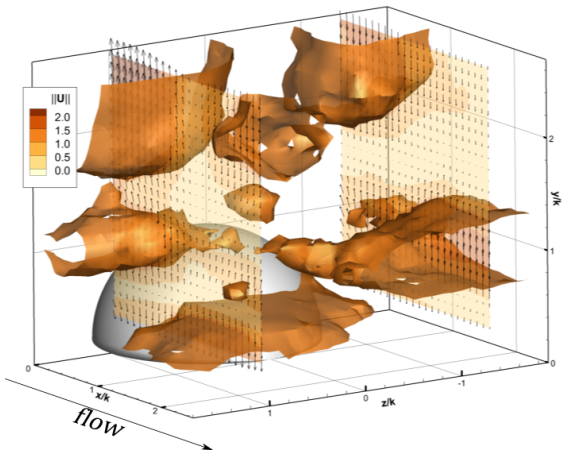

(f) Mode 6

Figure 5.8: The first six velocity modes shown with velocity magnitude $||\boldsymbol{U}||$ isosurfaces at 1.1 and a slice to show vector direction

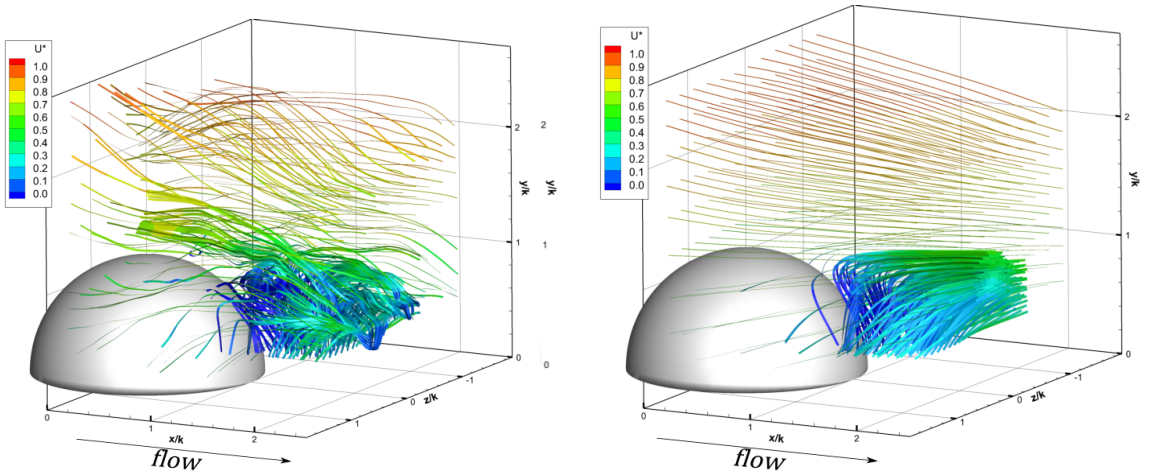

(a) 100% total energy

(b) 11% total energy

(c) 18% total energy

(d) 23% total energy

(e) 40% total energy

(f) 60% total energy

Figure 5.9: Reduced Order Projections of volume pair 756 with labeled total energy: (a) the complete volume; (b)-(f) projections using the first 2, 4, 6, 19, and 61 modes, respectively

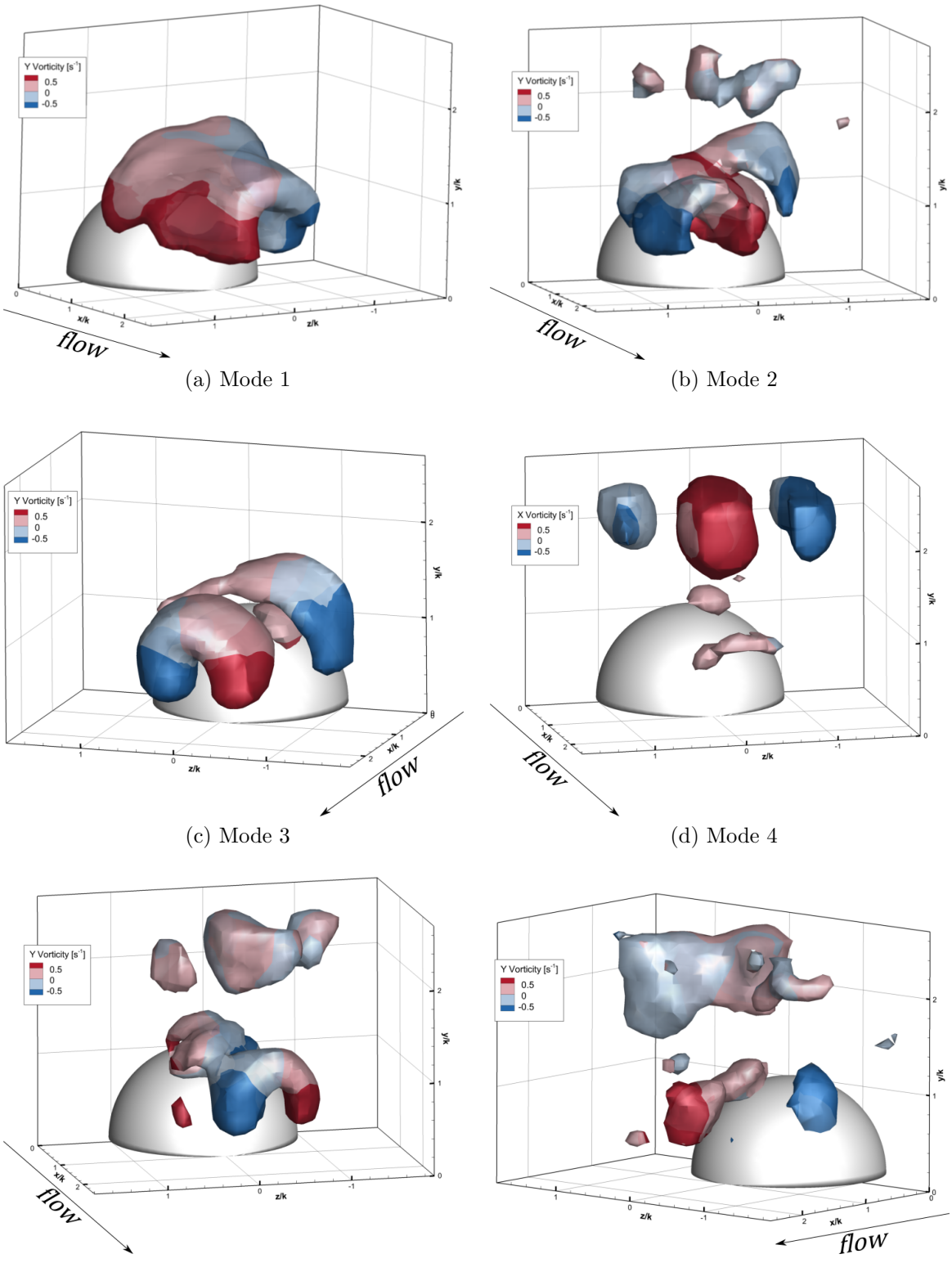

(a) Mode 1

(b) Mode 2

(c) Mode 3

(d) Mode 4

(e) Mode 5

(f) Mode 6

Figure 5.10: The first six vorticity modes shown with vorticity magnitude $||\boldsymbol{\omega}||$ isosurfaces at 1.1 which are colored by y vorticity or x vorticity, depending on which is more dominant

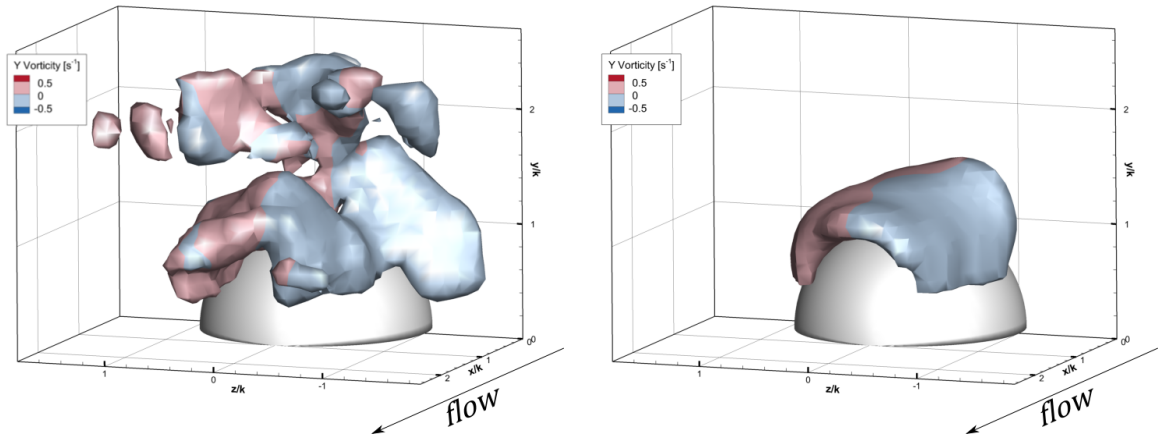

(a) 100% total enstrophy

(b) 6% total enstrophy

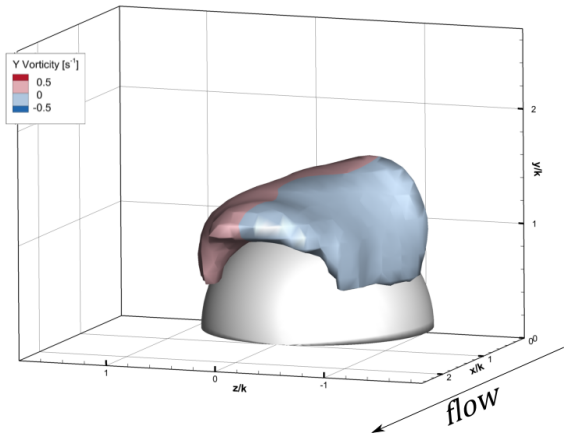

(c) 11% total enstrophy

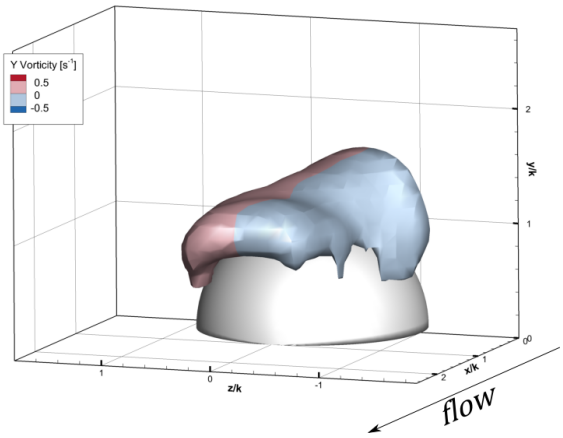

(d) 20% total enstrophy

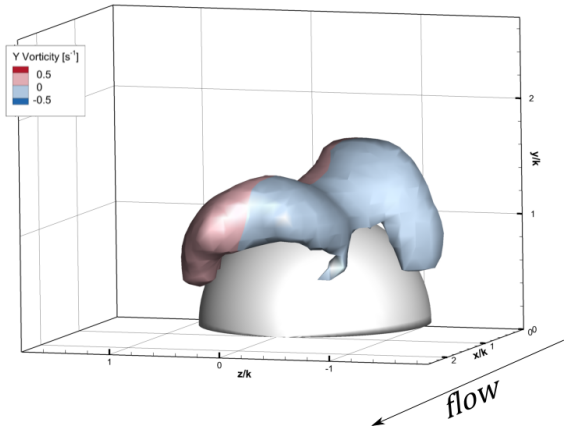

(e) 40% total enstrophy

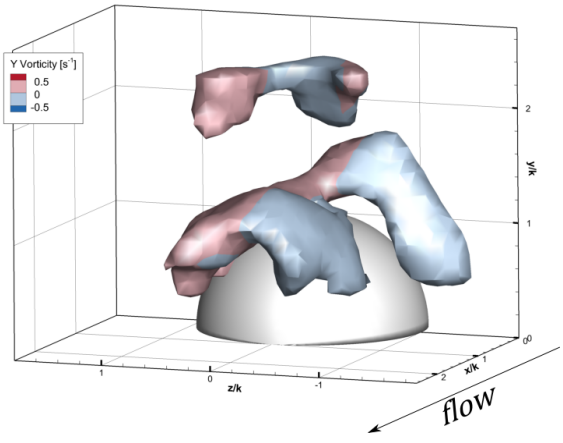

(f) 60% total enstrophy

Figure 5.11: Reduced Order Projections of volume pair 650 shown using isosurfaces of vorticity magnitude at 0.22, with labeled total enstrophy: (a) the complete volume; (b)-(f) projections using the first 4, 11, 18, 40, and 54 modes, respectively

Chapter 6

Conclusions and Future Work

The 3D topology of large-scale vortices in the wake of a hemisphere were measured and studied. An experiment was conducted using a refractive index matched flow facility and a plenoptic camera to make three-dimensional, three-component PIV measurements. This experiment signifies the first paring of Plenoptic PIV with a refractive index matched flow facility, as well as the first extensive application of plenoptic PIV for 3D flow measurements. A dataset of 986 instantaneous volumes were collected, with the goal of conducting a statistical analysis on the flow. The ensemble-averaged results show stratification in flow along the y direction, indicating the ability of the plenoptic camera to resolve particle motion at different depths along the optical axis. The ensemble-averaged vorticity shows an extended curved surface, stretching throughout the entire near-wake. A wide variety of flow phenomena are seen in the instantaneous volumes, some of which have been presented previously, showcasing spiraling legs of the shear layer, heavily perturbed overlying boundary layers, various sizes of recirculation regions, and both partial and full arch vortices.

The proper orthogonal decomposition was applied to both the instantaneous velocity and vorticity fields to better understand the flow physics. The POD of the velocity fields revealed a distinct connection between fluctuations in the upper boundary layer to changes in the near-wake region, a relationship that is seen in the most energetic modes. Conversely, the most energetic modes of the POD of the vorticity fields do not show such a relation, as structures are largely concentrated in the near-wake region. However, after the third mode, a relationship between fluctuations in x vorticity in the upper region of the boundary layer and y vorticity in the near-wake region is found in many lower energy modes. Arch-shaped structures are common throughout the higher energy modes, in agreement with the

arch-shaped vorticity structures seen in many of the instantaneous volumes. As a whole, the POD analysis suggests that the link between changes in velocity in the upper boundary layer is frequent, but the same coupling is not as strong with vorticity. Statistically, changes in vorticity are more dependent on fluctuations local to the near-wake. Overall, the POD modes describe a relationship between 3D structures in the near-wake region and the structures in the upper region of the boundary layer. The POD modes confirm plenoptic PIV as a viable technique for making statistically significant 3D velocity field measurements.

The presented flow features are shown to be linked to the size of the wake, however, it is unclear how the evolution of these flow features occur. One possibility is that over time, the recirculation region is stretched downstream, possibly linking the instantaneous volumes shown in Figure 5.5. At some point, the recirculation region would weaken and degrade; allowing the free stream flow to penetrate the recirculation region. This is the scenario seen in Figure 5.4. It is possible that an intermediate step between these two extremes would be the degradation of the recirculation region into a shed arch vortex, seen in Figure 5.6. However, time resolved information is necessary to properly confirm the relationship between the presented volumes, if any. This study has provided a starting point for future experiments, perhaps utilizing time resolved plenoptic PIV or a comparable technique, to further characterize the physics of this flow.

Bibliography

[1] Marc Levoy. Light fields and computational imaging. *Computer*, 39(8):46–55, 2006.

[2] Ronald Adrian and Jerry Westerweel. *Particle Image Velocimetry*. Cambridge Univeristy Press, 2011.

[3] M.P. Arroyo and C.A. Greated. Stereoscopic particle image velocimetry. *Measurement Science and Technology*, 2:1181–1186, 1991.

[4] G. E. Elsinga, Fulvio Scarano, B. Wieneke, B. W. Oudheusden, and B. W. Van Oudheusden. Tomographic particle image velocimetry. *Experiments in Fluids*, 41:933–947, 2006.

[5] J. Belden, T. T. Truscott, M. C. Axiak, and A. H. Techet. Three-dimensional synthetic aperture particle image velocimetry. *Measurement Science and Technology*, 21(12):125403, 2010.

[6] Timothy W Fahringer, Kyle P Lynch, and Brian S Thurow. Volumetric particle image velocimetry with a single plenoptic camera. *Measurement Science and Technology*, 26(11):1–25, 2015.

[7] K D Hinsch. Holographic particle image velocimetry. *Measurement Science & Technology*, 13:R61–R72, 2002.

[8] Sven F Herrmann and Klaus D Hinsch. Light-in-flight holographic PIV (LiFH-PIV) for wind- tunnel applications : Off-site reconstruction of deep- volume real particle images. *Measurement Science & Technology*, 15:1–9, 2004.

[9] C.E. Willert and M. Gharib. Three-dimensional particle imaging with a single camera. *Experiments in Fluids*, 12(6), apr 1992.

[10] G Blois, K T Christensen, J L Best, G Elliott, J Austin, C Dutton, M Bragg, M H Garcia, and B W Fouke. A versatile refractive-index-matched flow facility for studies of complex flow systems across scientific disciplines. In *50th AIAA Aero Sciences Meeting including the New Horizons Forum and Aerospace Exposition*, number January, pages 1–20, Nashville, Tennessee, 2012.

[11] David P. Stern and Mauricio Peredo. Thoughts on Ray Vibrations, 2010.

[12] Eh Adelson and Jr Bergen. The plenoptic function and the elements of early vision. *Computational models of visual ...*, pages 3–20, 1991.

[13] G Lippmann. Epreuves reversibles donnant la sensation du relief. *J. Phys. Theor. Appl.*, pages 921–925, 1908.

[14] Edward H. Adelson and John Y a Wang. Single lens stereo with a plenoptic camera. *IEEE Transactions on Pattern Analysis and Machine Intelligence*, 14(2):99–106, 1992.

[15] Kyle Lynch, T Fahringer, and B Thurow. Three-Dimensional Particle Image Velocimetry Using a Plenoptic Camera. *50th AIAA Aero Sciences Meeting including the New Horizons Forum and Aerospace Exposition*, (January):1–14, 2012.

[16] John L. Lumley. The structure of imhogeneous turbulence. *Atmospheric Turbulence and Wave Propogation*, pages 166–178, 1967.

[17] A. A. Townsend. *The Structure of Turbulent Shear Flow*. Cambridge Univeristy Press, 1956.

[18] Steven J. Leon. *Linear Algebra with Applications*. Pearson Learning Solutions, eighth edition, 2010.

[19] John David Logan. *Applied Mathematics*. John Wiley & Sons, Inc., third edition, 2006.

[20] Lindsay I Smith. A tutorial on Principal Components Analysis Introduction. *Statistics*, 51:52, 2002.

[21] Anindya (Penn State University) Chatterjee. An introduction to the proper orthogonal decomposition. *Computational Science Section Tutorial*, 2000.

[22] Holger Nobach, Cameron Tropea, Laurent Cordier, Jean-Paul Bonnet, Joël Delville, Jacques Lewalle, Marie Farge, Kai Schneider, and Ronald Adrian. Proper Orthogonal Decomposition: POD. In Cameron Tropea, John Foss, and Alexander Yarin, editors, *Springer Handbook of Experimental Fluid Mechanics*, chapter 22.4, pages 1346–1370. Springer, 2007.

[23] Philip Holmes, John L. Lumley, and Gal Berkooz. *Turbulence, Coherent Structures, Dynamical Systems and Symmetry*. Cambridge Univeristy Press, 1998.

[24] Lawrence Sirovich. Turbulence and the dynamics of coherent structures part i: coherent structures*. *Quarterly of Applied Mathematics*, XLV(3):561–571, 1987.

[25] W Jacobs. Flow behind a single roughness element. *Ing. Archives*, 7(36), 1938.

[26] Leslie SG Kovasznay. A new look at transition. In *Durand Centennial*, pages 161–172, 1960.

[27] P.S. Klebanoff, K.D. Tidstrom, and L M Sargent. The three-dimensional nature of boundary-layer instability. *Journal of Fluid Mechanics*, 12, 1961.

[28] Theodore Theodorson. The structure of turbulence. Technical report, The Institute for Fluid Dynamics and Applied Mathmatics, Univeristy of Maryland, 1954.

[29] M. S. Acarlar and C. R. Smith. A study of hairpin vortices in a laminar boundary layer. Part 1. Hairpin vortices generated by a hemisphere protuberance. *Journal of Fluid Mechanics*, 175:1, 1987.

[30] C.J. Baker. The laminar horseshoe vortex. *Journal of Fluid Mechanics*, 95(02):347–367, 1979.

[31] C.J. Baker. The turbulent horseshoe vortex. *Journal of Wind Engineering and Industrial Aerodynamics*, 6:9–23, 1980.

[32] E. Savory and N. Toy. The flow regime in the turbulent near wake of a hemisphere. *Experiments in Fluids*, 4:181–188, 1986.

[33] E. Savory and N. Toy. The separated shear layers associated with hemispherical bodies in turbulent boundary layers. *Journal of Wind Engineering and Industrial Aerodynamics*, 28(1-3):291–300, 1988.

[34] Michael Manhart. Vortex Shedding from a Hemisphere in a Turbulent Boundary Layer. *Theoretical and Computational Fluid Dynamics*, 12(1):1–28, 1998.

[35] Ian A. Carr and Michael W. Plesniak. Three-dimensional flow separation over a surface-mounted hemisphere in pulsatile flow. *Experiments in Fluids*, 57(1):9, 2016.

[36] M Fedrizzi, M Giacobello, J Soria, C Atkinson, and M Jones. Experimental Investigation of a Hemisphere in a Thin Flat Plate Boundary Layer. In *18th Australasian Fluid Mechanics Conference*, number December, pages 18–21, Launceston, Australia, 2012.

[37] M. M. Tavakol, M. Yaghoubi, and M. Masoudi Motlagh. Air flow aerodynamic on a wall-mounted hemisphere for various turbulent boundary layers. *Experimental Thermal and Fluid Science*, 34(5):538–553, 2010.

[38] Dongjoo Kim and Haecheon Choi. Laminar flow past a hemisphere. *Physics of Fluids*, 15(8):2457–2460, 2003.

[39] Stanislav Gordeyev and Eric Jumper. Fluid dynamics and aero-optics of turrets. *Progress in Aerospace Sciences*, 46(8):388–400, 2010.

[40] N. T. Hoang, O. K. Rediniotis, and D. P. Telionis. Dynamic character of the hemisphere-cylinder wake. *Experiments in Fluids*, 26(1989):415–422, 1999.

[41] H. J. Hussein and R. J. Martinuzzi. Energy balance for turbulent flow around a surface mounted cube placed in a channel. *Phys. Fluids*, 8(3):764–780, 1996.

[42] R. Martinuzzi and C. Tropea. The Flow Around Surface- Mounted , Prismatic Obstacles Placed in a Fully Developed Channel Flow. *Journal of Fluids Engineering*, 115:85–92, 1993.

[43] Seyed M. Hajimirzaie, Craig J. Wojcik, and James H J Buchholz. The role of shape and relative submergence on the structure of wakes of low-aspect-ratio wall-mounted bodies. *Experiments in Fluids*, 53(6):1943–1962, 2012.

Appendix A

Matlab POD Code

A.1 POD Snapshot Method

```
function  PODsnapshots(vectorsDir,numOfModes,indicies,loadC)
% Created by Kyle Johnson on 4/7/2016

% This code is a faster and better organized function of the three codes
% "prePOD.m", "snapshotsPOD", and "writePOD", which were controlled by the
% function "runningPOD." These functions were based off of code written by
% Kyle Lynch in 2008.

% The purpose of this function is to apply the proper orthogonal
% decomposition (POD) to 3D volumetric data and save the eigenmodes and
% which can be used to do reduced order modeling of the data

% PODsnapshots(vectorFolder,numOfModes,indicies,loadC)
% Definitiions:
%   vectorFolder
%       the directory where the vectors are stored, preferably in %04d
%       numbered format
%   numOfModes
%       the number of modes to calculate and save
%   indicies
%       the indicies that will be correlated, generally [4 5 6] for
%       veloctiy or [7 8 9] for vorticity. These are the indicies in the
%       .plt data file. (This code should also work for 2D data although it
%       has yet to be tested)
%   loadC
%       currently, the only option input is 'LoadC' which will load the
%       covariance matrix from file. C.mat and Vectors.mat need to be in
%       the appropaite folder which is the same as matDirOut


tic
fileContents        = dir([vectorsDir '\*.plt']);
numOfVecs           = numel(fileContents);


resultsDirOut   = [vectorsDir '\POD\'];
matDirOut       = [resultsDirOut '\Mat'];
printClock('Start','POD',resultsDirOut)
if ~exist('loadC','var')
    if ~exist(resultsDirOut,'dir')
```

```
41          mkdir(resultsDirOut)
42      end
43      if ~exist(matDirOut,'dir')
44          mkdir(matDirOut)
45      end
46
47      % Begin Vectorizing the data. The vector fields will now be collapsed to
48      % column vectors and the mean will be calculated
49
50      fprintf('Vectorizing Data:\t      ')
51      for vecInd          = 1:numOfVecs
52          fileID          = fopen([vectorsDir '\' fileContents(vecInd).name]);
53          header1         = fgetl(fileID);
54          header2         = fgetl(fileID);
55          header3         = fgetl(fileID);
56          vars            = numel(find(header2 == '"'))/2;
57          string          = repmat('%f ',[1 vars]);
58          data            = textscan(fileID,string,'delimiter',',');
59          fclose(fileID);
60          if vecInd       == 1
61              pts         = size(data{1},1)*numel(indicies);
62              Vectors     = zeros(pts,numOfVecs);
63          end
64          X               = cell(1,numel(indicies));
65          for ind         = 1:numel(indicies)
66              X{ind}      = data{indicies(ind)};
67          end
68          vec             = cell2mat(X);
69          Vectors(:,vecInd) = reshape(vec,pts,1);
70          fprintf('\b\b\b\b%4d',vecInd)
71      end
72
73      fprintf('\tComplete.\n')
74      %  The mean is subtracted from all the vectors.
75      fprintf('Subtracting Mean:\t      ')
76      VecAve = mean(Vectors,2);
77      vecAve = reshape(VecAve,[numel(X{1}),numel(indicies)]); %#ok<NASGU>
78      save([matDirOut '\VecAve'],'VecAve')
79      save([matDirOut '\Vectors'],'Vectors')
80      meanSubVectors = Vectors - repmat(VecAve,1,numOfVecs);
81      save([matDirOut '\meanSubVectors'],'meanSubVectors')
82      fprintf('\tComplete.\n')
83
84      fprintf('Creating Covariance Matrix:          ')
85      C = zeros(numOfVecs,numOfVecs);
86      for vecOuter    = 1:numOfVecs
87          fprintf('\b\b\b\b%4d',vecOuter)
88          X1          = meanSubVectors(:,vecOuter);
89          for vecInner = vecOuter:numOfVecs
90              X2                      = meanSubVectors(:,vecInner);
91              C(vecInner,vecOuter)    = sum(X1.*X2);
92              C(vecOuter,vecInner)    = C(vecInner,vecOuter);
93          end
94      end
```

```
95      fprintf('\t\r\tComplete.\n')
96      C = C/numOfVecs;
97      save([matDirOut '\C.mat'],'C')
98
99  else  % TO LOAD A COVARIANCE MATRIX AND VECTOR FILE TO CALCULATE MODES
100     fprintf('Loading Covarinace Matrix:      ')
101     laod([matDirOut '\C.mat'],'C')
102     load([matDirOut '\Vectors'],'Vectors')
103     fprintf('\tComplete.')
104 end
105
106 fprintf('Solving the Eigenvector/Eigenvalue Problem:     ')
107 [evectorC,evalueC]  = eig(C);
108 [lam,energyInd]     = sort(diag(evalueC),'descend');
109 evector             = evectorC(:,energyInd.');
110 lamNorm             = lam./sum(lam);
111 lamCum              = cumsum(lamNorm);
112
113 save([matDirOut '\lam.mat'],'lam')
114 save([matDirOut '\lamNorm.mat'],'lamNorm')
115 save([matDirOut '\lamCum.mat'],'lamCum')
116
117 energyPlotsPOD(resultsDirOut,lam,lamCum,lamNorm,numOfModes)
118
119 fprintf('\t\tComplete.\n')
120 fprintf('Compiling Modes:          ')
121
122 comma           = find(header3==',');
123 header3end      = header3(comma:end);
124 for modeInd     = 0:numOfModes
125     if modeInd == 0
126         mode = vecAve;
127     else
128         mode        = zeros(size(meanSubVectors,1),1);
129         for vecInd  = 1:numOfVecs
130             mode        = mode + evector(vecInd,modeInd)*meanSubVectors(:,
                    vecInd);
131         end
132         mode        = reshape(mode,[numel(X{1}),numel(indicies)]);
133     end
134     save([matDirOut '\mode' num2str(modeInd) '.mat'],'mode')
135
136     fileID      = fopen([resultsDirOut '\mode' num2str(modeInd) '.plt'],'wt');
137     fprintf(fileID,'%s\n',header1);
138     fprintf(fileID,'%s\n',header2);
139     header3     = ['ZONE T="mode' num2str(modeInd) '"' header3end];
140     fprintf(fileID,'%s\n',header3);
141     if indicies(1) == 4
142         for k = 1:size(mode,1)
143             fprintf(fileID,[string '\n'],data{1}(k),data{2}(k),data{3}(k),mode
                    (k,:));
144         end
145     else
146         zerop = zeros(1,indicies(1)-4);
```

```
147             for k = 1:size(mode,1)
148                 fprintf(fileID,[string '\n'],data{1}(k),data{2}(k),data{3}(k),
                        zerop,mode(k,:));
149             end
150         end
151         fclose(fileID);
152         fprintf('\b\b\b\b%4d',modeInd)
153     end
154     fprintf('\tComplete.\n')
155     fprintf('\n\tComputation Time:  %3.1f minutes\n',round(toc/60,1))
156     printClock('Stop','POD',resultsDirOut)
```

A.2 Reduced Order Projections

```
1   function [] = ReducedOrderProjections(vectorDir,cumEnergies,vectors,modeNums)
2   % created by Kyle Johnson 4/7/2016
3
4   % This code projects data onto the optimal basais created by
5   % "PODsnapshots.m" This basis is comprised of the collection modes.
6   % This code has tailored to work with "PODsnapshots.m"
7
8   % [] = ReducedOrderProjections(vectorFolder,cumEnegies,images,varargin)
9   % Definitiions:
10  %  vectorFolder
11  %       the directory where the vectors are stored, preferably in %04d
12  %       numbered format
13  %   cumEnergies
14  %       the cumaltive energy that the prjections will have. This can be a
15  %       single value, or multiple values, for which the code will loop for
16  %       numel(cumIndicies). These values are a percenatage and should be
17  %       entered as intergers not decimals  e.g. [10, 20]
18  %   vectors
19  %       these are the vectors that will be projected onto the basis.
20  %       **NOTE** these should be the vector numbers not the image numbers,
21  %        if your data set is of the form {"0002.plt", "0004.plt",
22  %       "0006.plt",..., "2000.plt"} image 0004 would be identified by
23  %       vector 0002. e.g. [2, 50, 100:150]
24
25
26
27
28
29
30  PODdir          = [vectorDir '\POD'];
31  matDir          = [PODdir '\Mat'];
32  printClock('Start','POD Projection',[PODdir '\Projections'])
33
34  for energyInd = 1:numel(cumEnergies)
35      cumEnergy       = cumEnergies(energyInd);
36      fprintf('Projecting at %2d percent of Cumlative Energy\n',cumEnergy)
37
38
39
40
```

```
41
42      % load vectors
43      fprintf('Loading vectors:\t')
44      load([matDir '\meanSubVectors'])
45      load([matDir '\VecAve'])
46      fprintf('\t\t\t\tComplete.\n')
47
48      % Calculate the number of modes needed
49      load([matDir '\lamCum'])
50      numOfModes = find(lamCum>cumEnergy/100,1);
51      fprintf('Using %d modes',numOfModes)
52
53      % Load Modes
54      pts             = size(meanSubVectors,1);
55      fprintf('\nLoading Modes:      ')
56      Modes           = zeros(pts,numOfModes);
57      for m           = 1:numOfModes
58          load([matDir '\mode' num2str(m)]);
59          Modes(:,m)  = reshape(mode(:,:,:),[pts,1]);
60          clearvars mode
61          fprintf('\b\b\b\b%4d',m)
62      end
63      fprintf('\t\t\t\t\tComplete.\n')
64      % Load a sample .plt for formatting
65      fileContents    = dir([vectorDir '\*.plt']);
66      fileID          = fopen([vectorDir '\' fileContents(1).name]);
67      header1         = fgetl(fileID);
68      header2         = fgetl(fileID);
69      header3         = fgetl(fileID);
70      vars            = numel(find(header2 == '"'))/2;
71      string          = repmat('%f ',[1 vars]);
72      comma           = find(header3==',');
73      header3end      = header3(comma:end);
74      data            = textscan(fileID,string,'delimiter',',');
75      X               = data{1};
76      Y               = data{2};
77      Z               = data{3};
78      fclose(fileID);
79      % Calcualte the redueced order approximation and write data out
80      fprintf('Reduced Order Approximations:      ')
81      a               = zeros(numOfModes,1);
82      for modeInd     = 1:size(vectors,2)
83          for vecInd      = 1:size(vectors,1)
84              V           = meanSubVectors(:,vectors(vecInd,modeInd));
85              RO          = VecAve;%/sum(VecAve.*VecAve);
86              for m       = 1:numOfModes
87                  M       = Modes(:,m);
88                  a(m)    = sum(M.*V)/sum(M.*M); % time coef
89                  RO      = RO + a(m)*M; % reduced order
90              end
91              RO          = reshape(RO,[size(X),3]);
92              % write data out
93              projDirOut      = [PODdir '\Projections\mode' num2str(modeNums(
                    modeInd))];
```

```
94                  if exist(projDirOut,'dir') == 0;
95                      mkdir(projDirOut)
96                  end
97                  textName = ['ROM' num2str(numOfModes) '_CE' num2str(cumEnergy) '
                        __' num2str(vectors(vecInd,modeInd))];
98                  fileNameOut = [projDirOut '\' textName '.plt'];
99                  header3 = ['ZONE T="' textName '"' header3end];
100                 fileID = fopen(fileNameOut,'wt');
101                 fprintf(fileID,'%s\n',header1);
102                 fprintf(fileID,'%s\n',header2);
103                 fprintf(fileID,'%s\n',header3);
104                 if vars ==6
105                     for k = 1:size(X,1)
106                         fprintf(fileID,'%f,%f,%f,%f,%f,%f\n',X(k),Y(k),Z(k),RO(k
                                ,1),RO(k,2),RO(k,3));
107                     end
108                 else
109                     for k = 1:size(X,1)
110                         fprintf(fileID,'%f,%f,%f,%f,%f,%f\n',X(k),Y(k),Z(k),0,0,0,
                                RO(k,1),RO(k,2),RO(k,3));
111                     end
112                 end
113                 fclose(fileID);
114             end
115             fprintf('\b\b\b\b%4d',modeInd)
116         end
117         fprintf('\tComplete.\n\n')
118 end
119 printClock('Stop','POD Projection',[PODdir '\Projections'])
```

Appendix B
Additional POD Modes

B.1 Velocity POD Modes

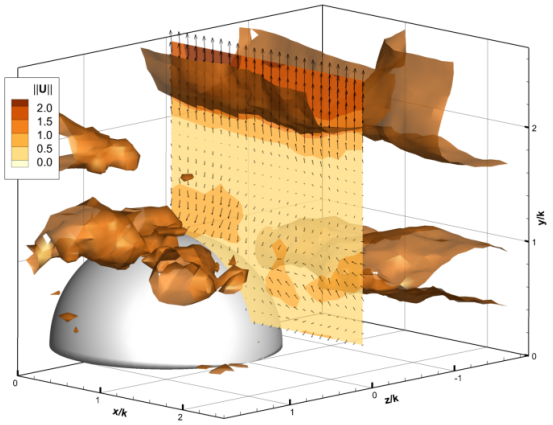

(a) Mode 7

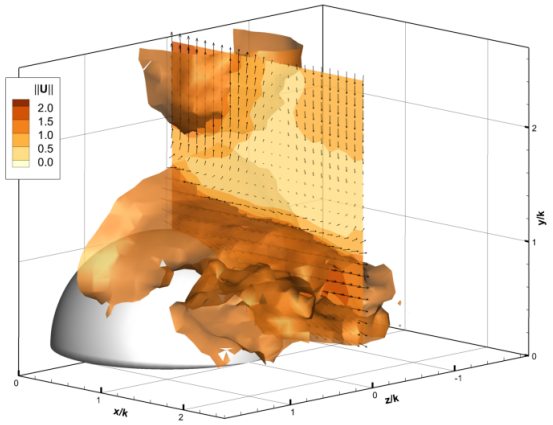

(b) Mode 8

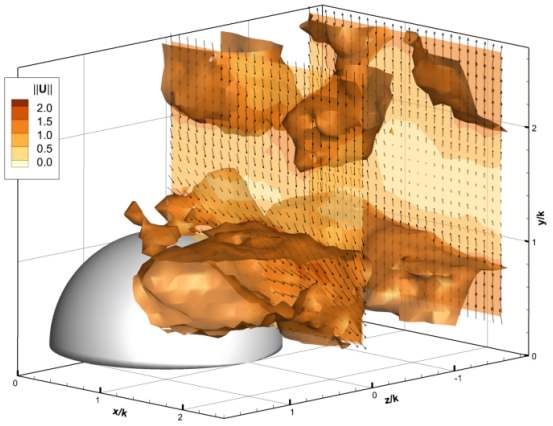

(c) Mode 9

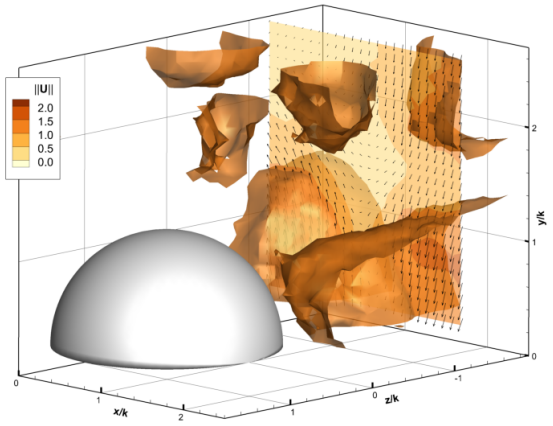

(d) Mode 10

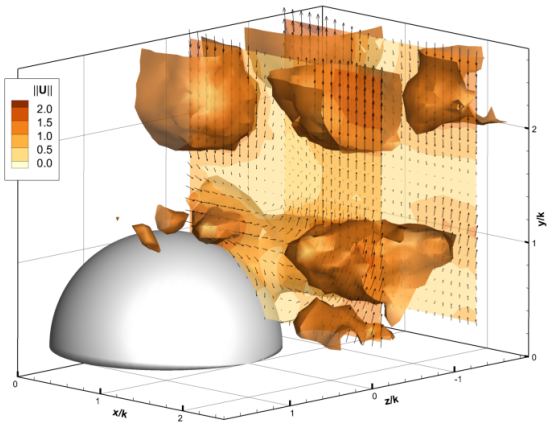

(e) Mode 11

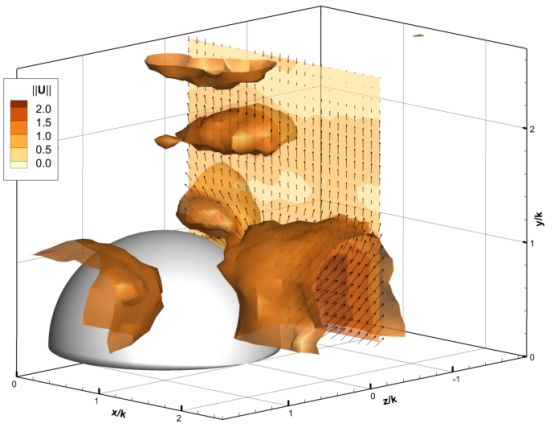

(f) Mode 12

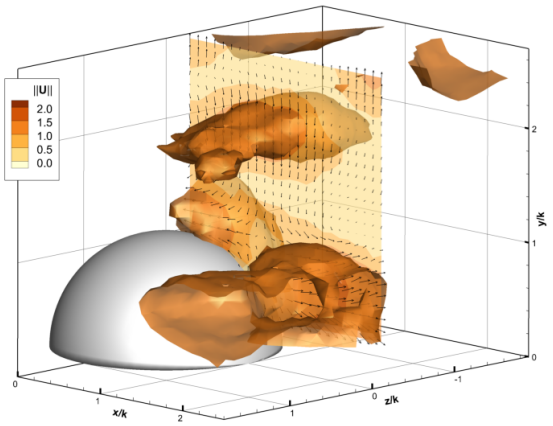

(g) Mode 13

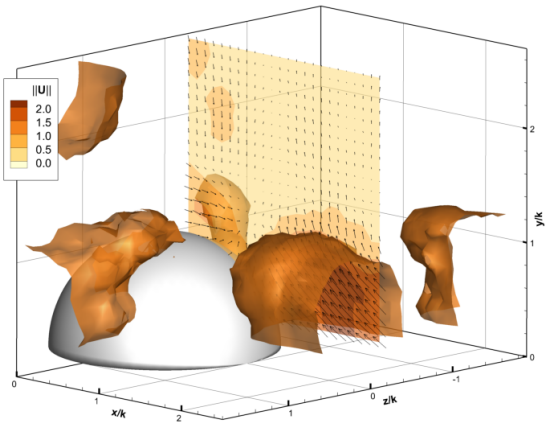

(h) Mode 14

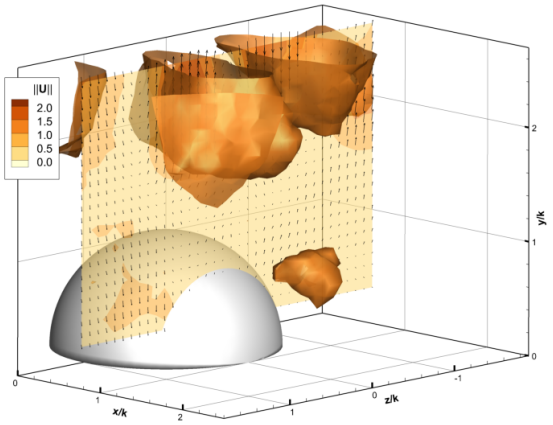

(i) Mode 15

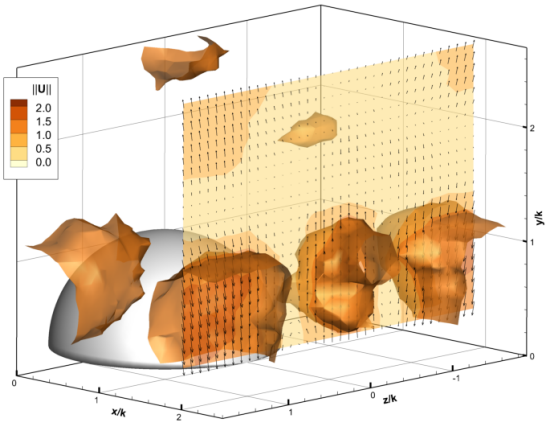

(j) Mode 16

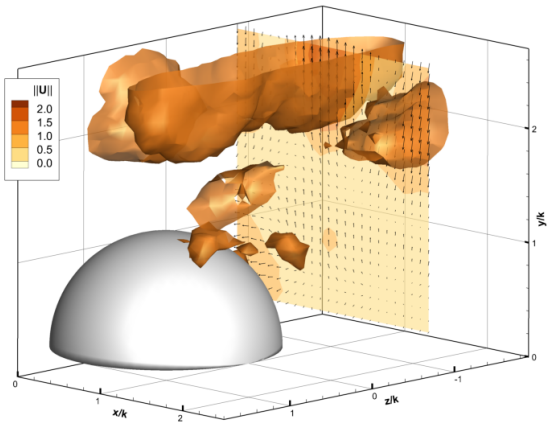

(k) Mode 17

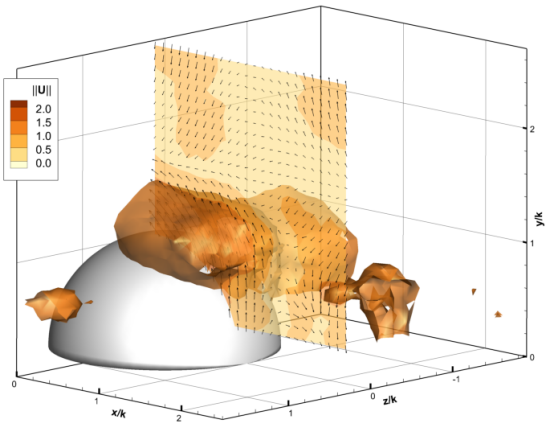

(l) Mode 18

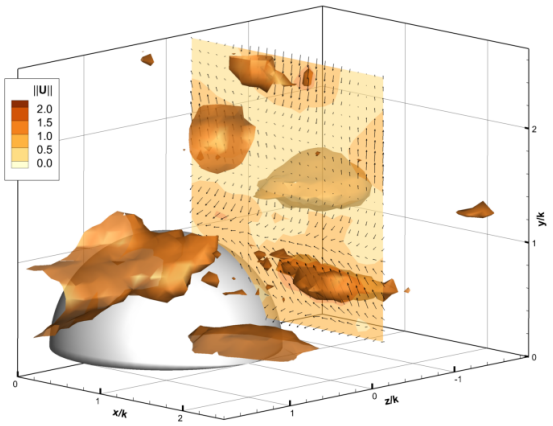

(m) Mode 19

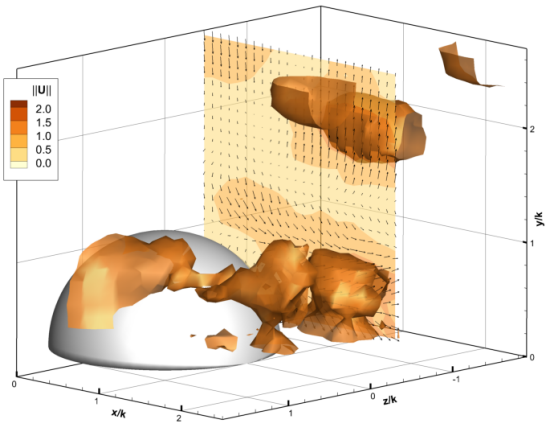

(n) Mode 20

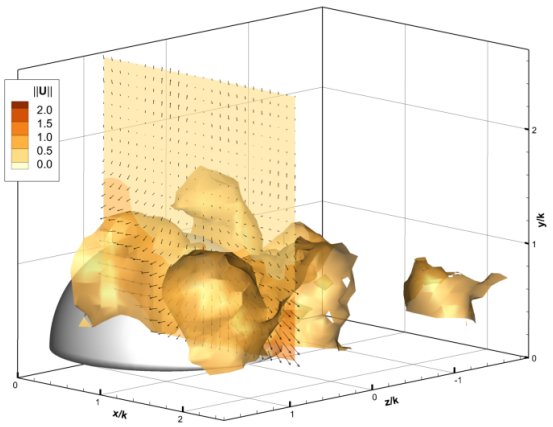

(o) Mode 25

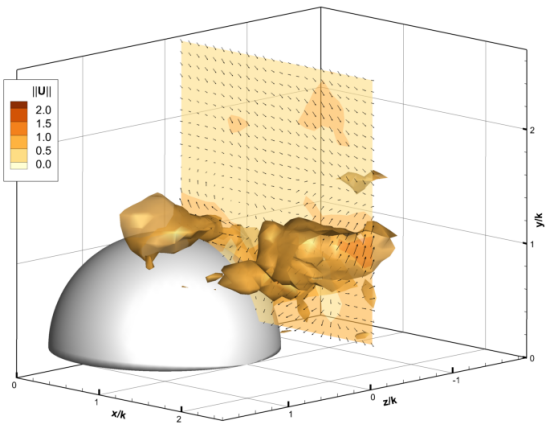

(p) Mode 30

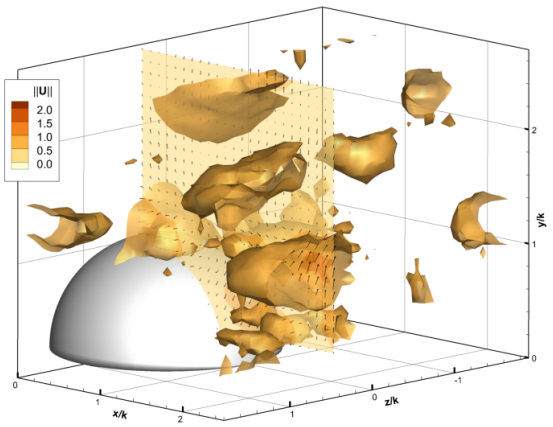

(q) Mode 50

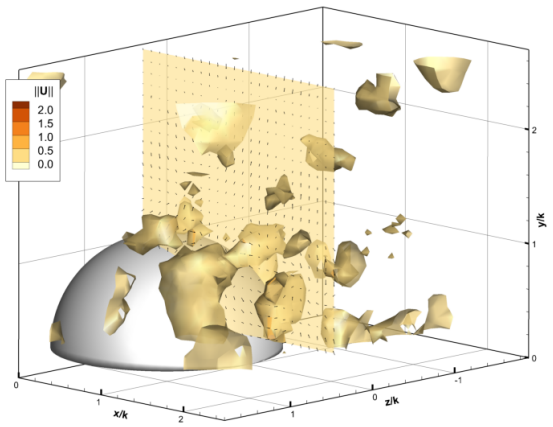

(r) Mode 100

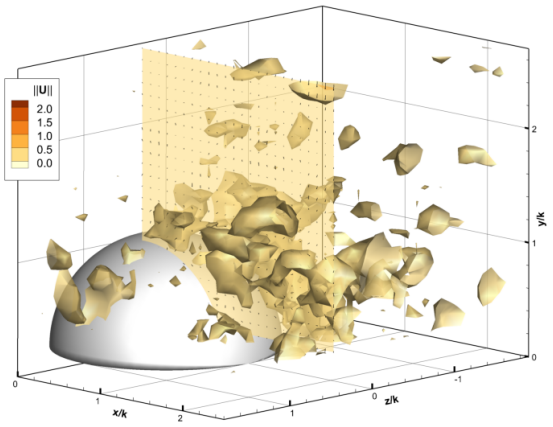

(s) Mode 200

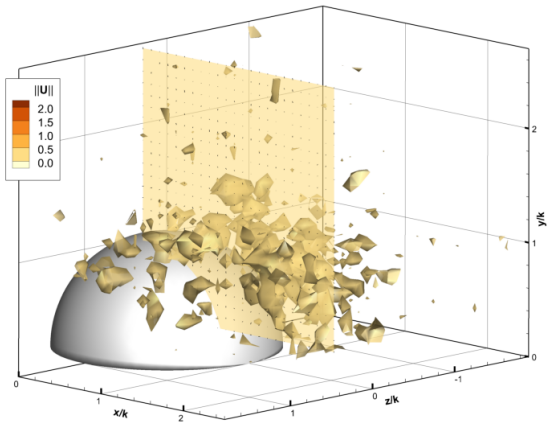

(t) Mode 500

Figure B.1: Additional POD modes of velocity are shown using slices of velocity magnitude and isosurfaces of velocity magnitude shown at the following thresholds: (a)-(n) Mode 7 - 20 with isosurfaces at 1.1; (o)-(p) Mode 25 and 30 with isosurfaces at 0.9; (q) Mode 50 with isosurfaces at 0.6; (r) Mode 100 with isosurfaces at 0.5; (s) Mode 200 with isosurfaces at 0.3; (t) Mode 500 with isosurfaces at 0.2

B.2 Vorticity POD Modes

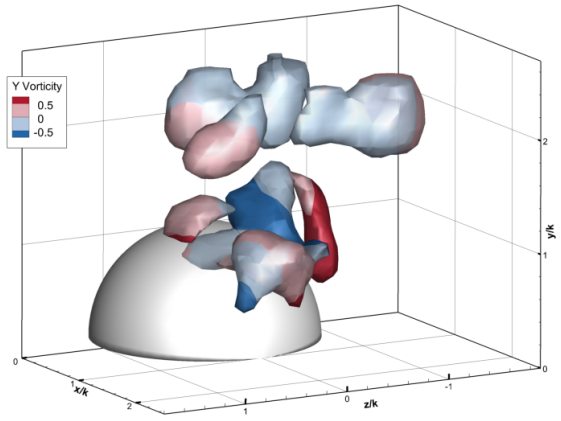

(a) Mode 7

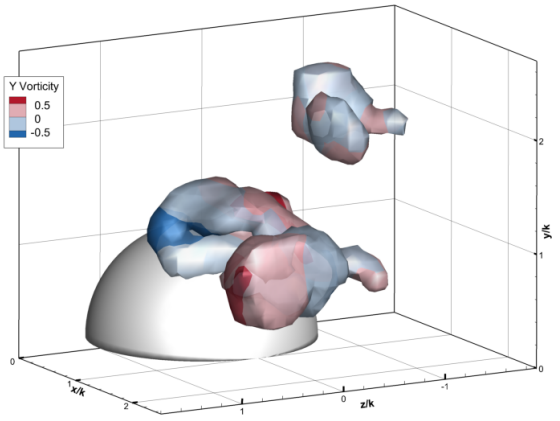

(b) Mode 8

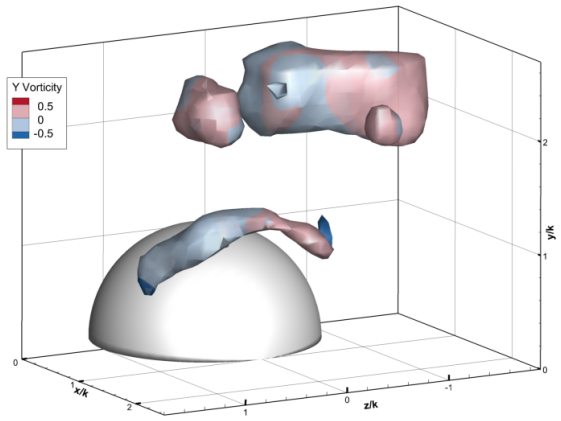

(c) Mode 9

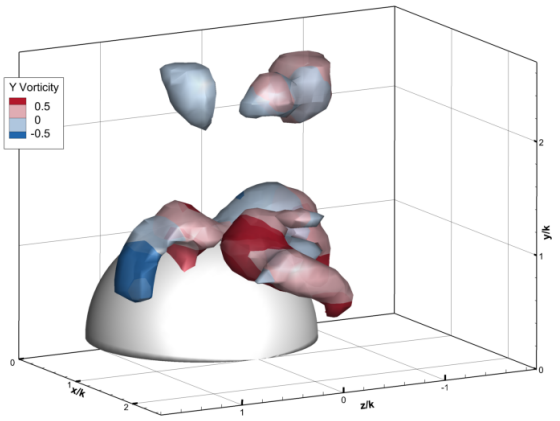

(d) Mode 10

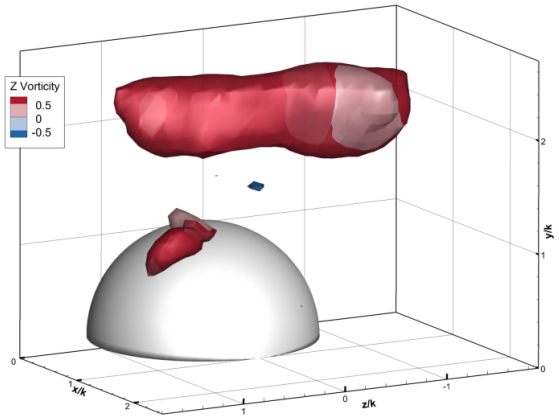

(e) Mode 11

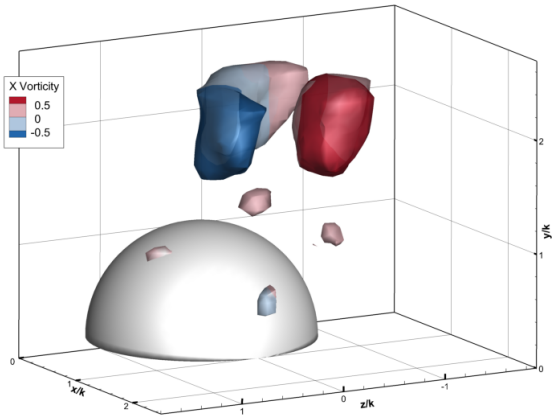

(f) Mode 12

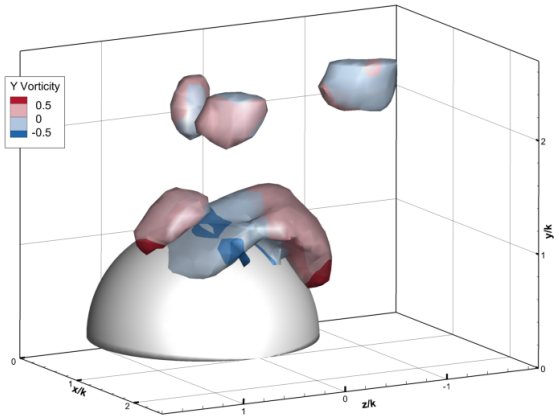

(g) Mode 13

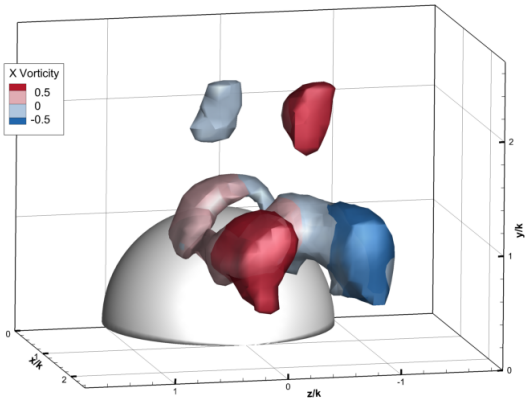

(h) Mode 14

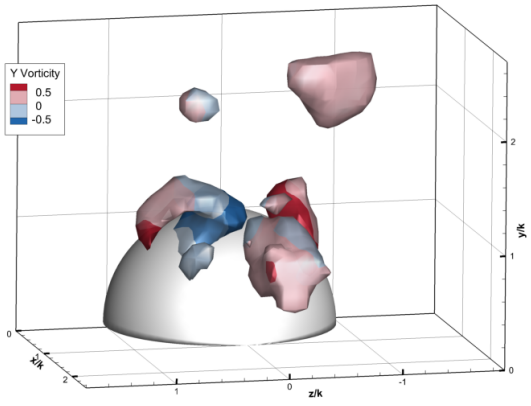

(i) Mode 15

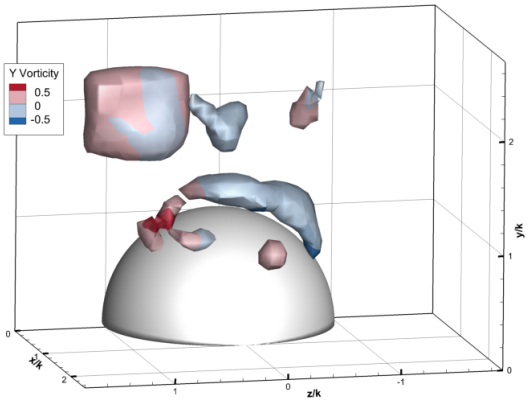

(j) Mode 16

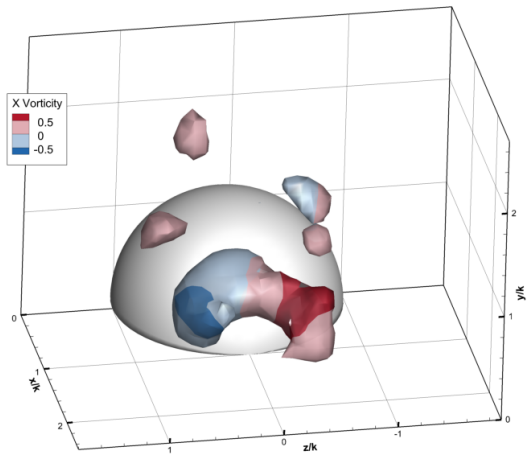

(k) Mode 17

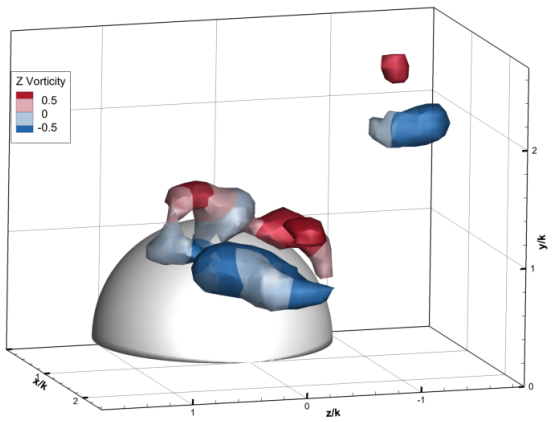

(l) Mode 18

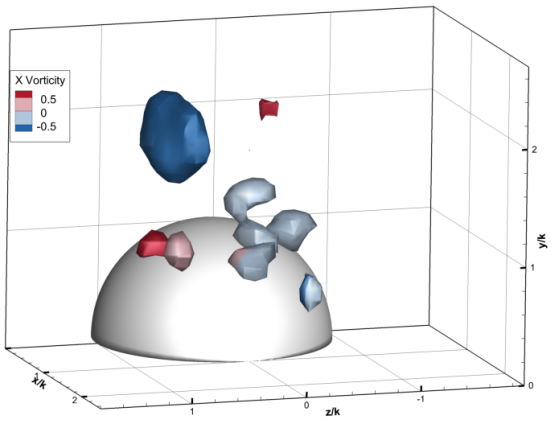

(m) Mode 19

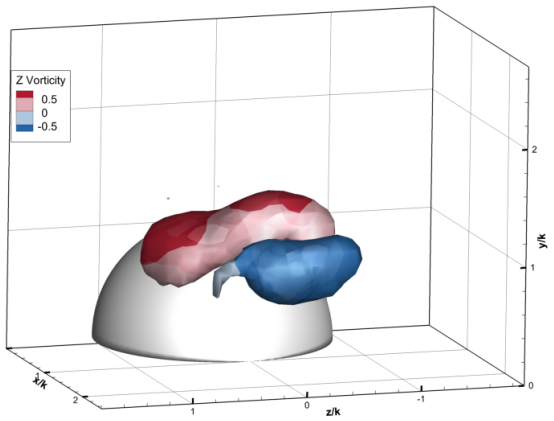

(n) Mode 20

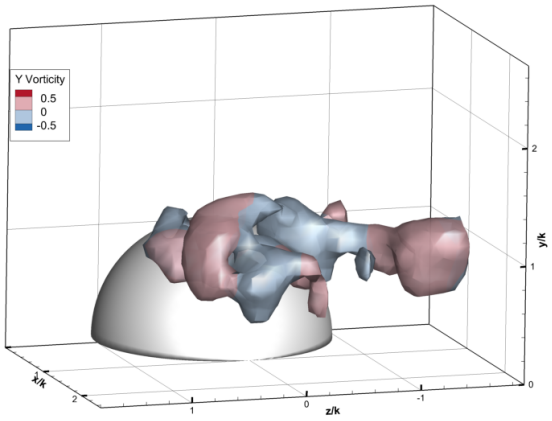

(o) Mode 25

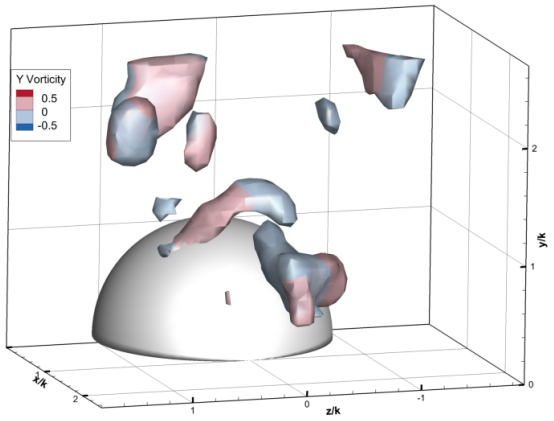

(p) Mode 30

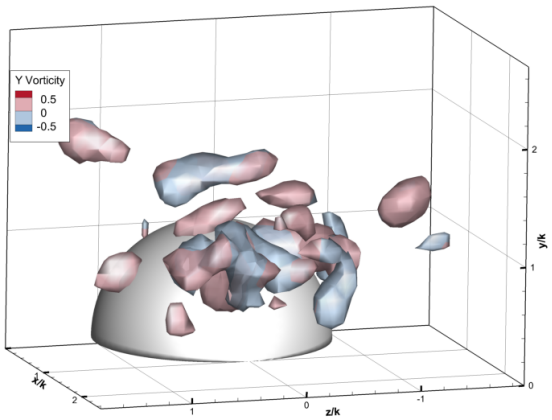

(q) Mode 50

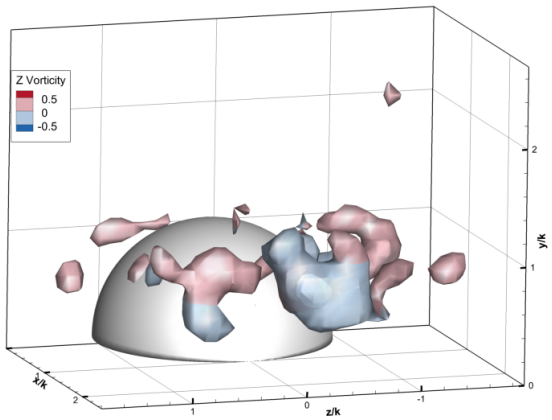

(r) Mode 100

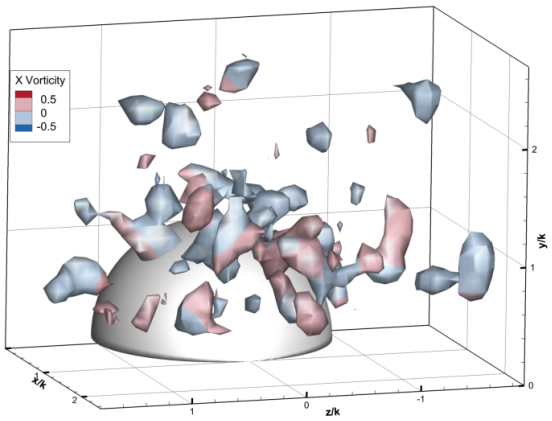

(s) Mode 200

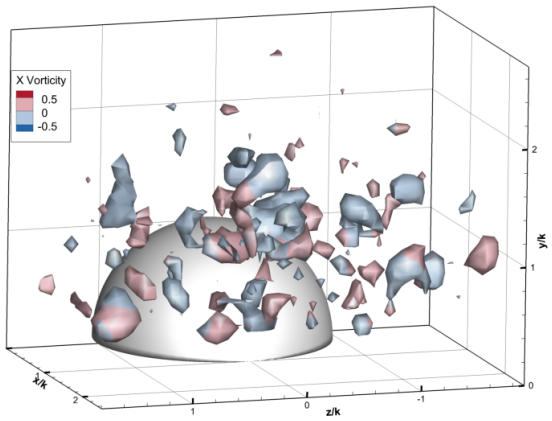

(t) Mode 500

Figure B.2: Additional POD modes of vorticity are shown using isosurfaces of vorticity magnitude at the following thresholds, colored by the most dominant vorticity component: (a)-(n) Mode 7 - 20 with isosurfaces at 0.6; (o)-(p) Mode 25 and 30 with isosurfaces at 0.5; (q) Mode 50 with isosurfaces at 0.4 (r) Mode 100 with isosurfaces at 0.3; (s) Mode 200 with isosurfaces at 0.2; (t) Mode 500 with isosurfaces at 0.1